J Nonlinear Sci
DOI 10.1007/s00332-015-9279-0

Journal of Nonlinear Science

From Canards of Folded Singularities to Torus Canards in a Forced van der Pol Equation

John Burke[1,3] · **Mathieu Desroches**[4] · **Albert Granados**[2] · **Tasso J. Kaper**[1] · **Martin Krupa**[4] · **Theodore Vo**[1]

Received: 3 April 2015 / Accepted: 31 October 2015

Abstract In this article, we study canard solutions of the forced van der Pol equation in the relaxation limit for low-, intermediate-, and high-frequency periodic forcing. A central numerical observation made herein is that there are two branches of canards in parameter space which extend across all positive forcing frequencies. In the low-frequency forcing regime, we demonstrate the existence of primary maximal canards induced by folded saddle nodes of type I and establish explicit formulas for the parameter values at which the primary maximal canards and their folds exist. Then, we turn to the intermediate- and high-frequency forcing regimes and show that the forced van der Pol possesses torus canards instead. These torus canards consist of long segments near families of attracting and repelling limit cycles of the fast system, in alternation. We also derive explicit formulas for the parameter values at which the maximal torus canards and their folds exist. Primary maximal canards and maximal torus canards correspond geometrically to the situation in which the persistent manifolds near the family of attracting limit cycles coincide to all orders with the persistent manifolds that lie near the family of repelling limit cycles. The formulas derived for the folds of maximal canards in all three frequency regimes turn out to be representations of a

Communicated by Alan R. Champneys.

✉ Tasso J. Kaper
tasso@math.bu.edu

1 Department of Mathematics and Statistics, Boston University, 111 Cummington Mall, Boston, MA 02215, USA

2 Department of Applied Mathematics and Computer Science, Technical University of Denmark, Building 303B, 2800 Kongens Lyngby, Denmark

3 Present Address: MSCI, Inc., 2100 Milvia Street, Berkeley, CA 94704, USA

4 NeuroMathComp Project-Team, Inria Sophia-Antipolis Research Centre, 2004 route des Lucioles, BP93, 06902 Sophia Antipolis cedex, France

Published online: 20 November 2015

single formula in the appropriate parameter regimes, and this unification confirms the central numerical observation that the folds of the maximal canards created in the low-frequency regime continue directly into the folds of the maximal torus canards that exist in the intermediate- and high-frequency regimes. In addition, we study the secondary canards induced by the folded singularities in the low-frequency regime and find that the fold curves of the secondary canards turn around in the intermediate-frequency regime, instead of continuing into the high-frequency regime. Also, we identify the mechanism responsible for this turning. Finally, we show that the forced van der Pol equation is a normal form-type equation for a class of single-frequency periodically driven slow/fast systems with two fast variables and one slow variable which possess a non-degenerate fold of limit cycles. The analytic techniques used herein rely on geometric desingularisation, invariant manifold theory, Melnikov theory, and normal form methods. The numerical methods used herein were developed in Desroches et al. (SIAM J Appl Dyn Syst 7:1131–1162, 2008, Nonlinearity 23:739–765 2010).

Keywords Folded singularities · Canards · Torus canards · Torus bifurcation · Mixed-mode oscillations

Mathematics Subject Classification Primary: 34E17 · 34E15 · 34A26 · 70K70 · Secondary: 34E13 · 34D15 · 34C29 · 34C45 · 37G15 · 92C20 · 70K43

1 Introduction

The forced van der Pol (fvdP) equation is a fundamental model for oscillatory processes in physics, electronics, biology, neurology, sociology, and economics. Possessing strong nonlinear damping effects, it is the prototype of a forced relaxation oscillator, exhibiting slow and fast timescales, see Bold et al. (2003), Cartwright and Littlewood (1945), Cartwright (1950), Flaherty and Hoppensteadt (1978), Haiduc (2009), Han and Bi (2012), Levi (1981), Levinson (1949), Sekikawa et al. (2005), van der Pol (1920), and van der Pol (1927). The equations may be formulated as

$$\begin{aligned} x' &= y - f(x), \\ y' &= \varepsilon(-x + a + b\cos\theta), \\ \theta' &= \omega, \end{aligned} \tag{1}$$

where the prime denotes the derivative with respect to the fast time variable τ, $f(x) = \frac{1}{3}x^3 - x$, and $0 < \varepsilon \ll 1$. The external signal, $a + b\cos\theta$, models a time-periodic driving force with drive frequency $\omega > 0$. Throughout this article, we will work with the form of the system given by (1), as it allows us to explore the full range of forcing frequencies $\omega > 0$.

A number of detailed studies of the fvdP equation (1) have been carried out in the low-frequency forcing regime, $\omega = \mathcal{O}(\varepsilon)$, see Bold et al. (2003), Guckenheimer et al. (2003), Han and Bi (2012), and Szmolyan and Wechselberger (2004). We cite Bold et al. (2003) in particular, which presents a detailed analysis of the folded saddle singularities and their attendant canards. In the context of excitable systems (in particular,

neuronal models), the folded saddle maximal canard plays the role of an excitability threshold manifold, locally dividing trajectories between those that jump at the fold to a different attracting manifold and those that do not Mitry et al. (2013), Wechselberger et al. (2014). This is also true in planar neuronal systems where solutions containing maximal canard segments correspond to excitability thresholds both in the case of type I neurons (integrators) and type II neurons (resonators) (Desroches et al. 2013; Izhikevich 2000). More generally, the canards induced by folded singularities (of node, saddle, and saddle-node types) have also been studied in models of neuronal dynamics (Rotstein et al. 2008; Rubin and Wechselberger 2008; Teka et al. 2011) and in many other systems, see for example Benoît (1990), Brøns et al. (2006), Desroches et al. (2008), Desroches et al. (2012), Krupa and Wechselberger (2010), Vo and Wechselberger (2015), Wechselberger (2005), Wechselberger (2012), Wechselberger et al. (2014).

In this article, we examine the fvdP equation (1) in three different regimes of forcing frequencies: low frequency ($\omega = \mathcal{O}(\varepsilon)$), intermediate frequency ($\omega = \mathcal{O}(\sqrt{\varepsilon})$), and high frequency ($\omega = \mathcal{O}(1)$). In each regime, we study the canard solutions that the fvdP equation (1) exhibits.

We begin in the low-frequency regime. First, we briefly apply the theory of folded singularities to (1), to identify the different types of folded singularities that it exhibits in this regime. We place special emphasis on folded saddle-node singularities of type I (FSN I), which are known to generate a number of different types of canard solutions, see Sect. 2.

The graph of the fast nullcline, $y = f(x)$, of system (1) with $\varepsilon = 0$ plays a central role in understanding the system dynamics. We are especially interested in the middle repelling branch and the attracting branch on the right, respectively, of the graph. Let S_r denote the two-dimensional manifold formed by rotating the (middle) repelling branch through one complete revolution in the angle $\theta : [0, 2\pi)$, and similarly let S_a be the two-dimensional manifold formed by rotating the (right) attracting branch through one complete revolution in θ. In the low-frequency regime of (1), Fenichel theory (Fenichel 1979; Jones 1995) guarantees that, when ε is sufficiently small, there exist two-dimensional, locally invariant manifolds S_r^ε and S_a^ε near S_r and S_a, respectively, away from the fold regions. In the low-frequency forcing regime, these persistent manifolds are referred to as slow manifolds, since the dynamics on them is slow in y and θ.

Canards of folded singularities are orbits that have a long segment close to S_a^ε, pass through a neighbourhood of the folded singularity, and then have a long segment near S_r^ε. These canards are divided into two classes: primary and secondary. There are two primary canards of folded singularities: strong and weak, both of which pass directly through a neighbourhood of the folded singularity. The weak canard plays the role of the axis of rotation for the secondary canards, which oscillate in a neighbourhood of the folded singularity. Secondary canards are indexed by the number of loops they make around the weak canard and by the value of the y-intercepts of the solutions during the nearly horizontal jumps that occur from a neighbourhood of S_r^ε back to a neighbourhood of S_a^ε. The lengths of the canard orbit segments on S_r^ε depend on the parameter values; and there are curves of parameter values along which the segment near S_r^ε has maximal length, going all the way up to the other fold curve. These canards

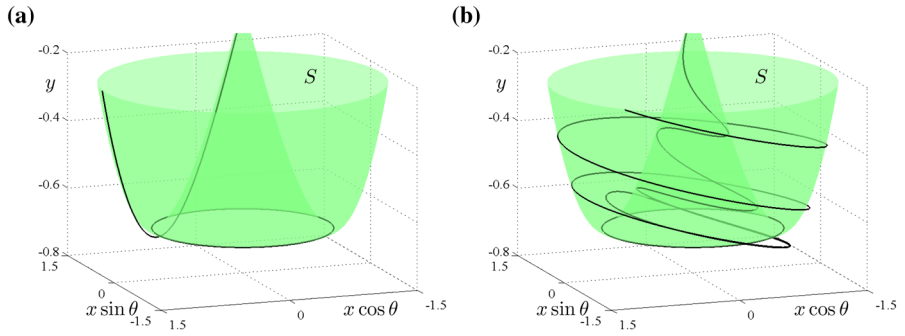

Fig. 1 **a** Segment of a primary maximal canard solution of (1), and **b** segment of a maximal torus canard solution of (1). Both have long segments near the family of attracting limit cycles (outer portion of the green surface) and near the family of repelling limit cycles (inner portion of the green surface). Here, $a = 0.997$, $b = 0.994$, $\varepsilon = 0.02$, and **a** $\omega = 0.001$ and **b** $\omega = 0.3$

are referred to as maximal canards; see Fig. 1a for a representative primary maximal canard. They are determined geometrically by the parameter values for which S_r^ε and S_a^ε agree to all orders in ε, in a manner analogous to the maximal limit cycle canards in the classical, planar van der Pol equation, recall (Benoit et al. 1981; Diener 1984; Eckhaus 1983). Within each family of canards, there is one maximal canard.

The following is the first main result of this article:

Theorem 1.1 (Low-frequency forcing) *Let $\omega = \varepsilon\,\overline{\omega}$, where $\overline{\omega} = \mathcal{O}(1)$, and let $b = \mathcal{O}(\sqrt{\varepsilon})$. Then, there exists an $\varepsilon_0 > 0$ such that for all $0 < \varepsilon < \varepsilon_0$, there are two curves in the $(a, \overline{\omega})$ parameter plane given by*

$$a = 1 - \frac{\varepsilon}{8} \pm b \exp\left(-\frac{\varepsilon\,\overline{\omega}^2}{2}\right), \tag{2}$$

emanating from the points $(\overline{\omega}, a) = (0, 1 - \frac{\varepsilon}{8} \pm b)$, along which the system (1) has folds of primary maximal canards. Moreover, for each $\mathcal{O}(1)$ value of $\overline{\omega}$, the system (1) has two primary maximal canards for every value of a in the interval between the points on these fold curves. Finally, there are no primary maximal canards for values of a outside the closures of these intervals.

This first theorem is established by using the geometric desingularisation method, also known as the blow-up method (Dumortier and Roussarie 1996, 2001; Krupa and Szmolyan 2001), to inflate the FSN I points into hyperspheres and then by employing invariant manifold theory and Melnikov theory in the appropriate coordinate charts, see Sect. 3.

Next, we show that system (1) has torus canards both in the intermediate-frequency forcing regime, in which (1) has three timescales, with x fast, θ intermediate, and y slow, and in the high-frequency forcing regime in which (1) is a two-fast (x, θ) and one-slow system (y). Torus canards are a relatively new type of canard solution discovered in a model of neuronal activity in Purkinje cells (Kramer et al. 2008). They consist of long segments near families of attracting and repelling limit cycles of the fast

system, in alternation. Torus canards have recently been shown to exist in a broad array of models, including in three models of neuronal bursting, see Burke et al. (2012): the Hindmarsh–Rose model, the Morris–Lecar–Terman system, and the Wilson–Cowan–Izhikevich equations; in a model of elliptic bursters, where the torus canards are rotated versions of limit cycle canards of a planar system (Izhikevich 2001); in a rotated van der Pol-type model system (Benes et al. 2011); as well as more recently in a model of respiratory rhythm generation in a pre-Bötzinger complex (Roberts et al. 2014). The significance of torus canards in these neuronal models is that they play a central role in the transition between periodic spiking and bursting of different types.

In the intermediate- and high-frequency regimes of (1), Fenichel theory (Fenichel 1979; Jones 1995) also guarantees that, when ε is sufficiently small, there exist two-dimensional, locally invariant manifolds near S_r and S_a, away from the fold regions. We again denote these by S_r^ε and S_a^ε and label them as persistent manifolds. However, it is crucial to observe that these persistent manifolds are no longer slow manifolds in these regions. Instead, the orbits of (1) on these persistent manifolds exhibit two timescales, with fast rotation due to the limit cycles, as well as slow drift in the vertical direction, down S_a^ε and up along S_r^ε.

Torus canards are orbits of (1) in the intermediate- and high-frequency regimes that have long segments near S_a^ε, spiral through a neighbourhood of the fold curve of limit cycles, and then have a long segment near S_r^ε. The lengths of time that torus canards spiral around near S_a^ε and S_r^ε depend on the system parameters, and for system (1) there are curves of parameter values along which the time spent near S_r^ε is maximal, with the orbits spiralling all the way up S_r^ε. These are defined to be maximal torus canards, in analogy with the maximal limit cycle canards of the unforced van der Pol oscillator. A representative maximal torus canard is shown in Fig. 1b.

For system (1) in the intermediate-frequency regime, we prove the following theorem:

Theorem 1.2 (Intermediate-frequency forcing) *Let $\omega = \sqrt{\varepsilon}\Omega$, where $\Omega = \mathcal{O}(1)$, and let $b = \mathcal{O}(\varepsilon)$. Then, there exists an $\varepsilon_0 > 0$ such that for all $0 < \varepsilon < \varepsilon_0$, there are two curves in the (a, Ω) parameter plane given by*

$$a = 1 - \frac{\varepsilon}{8} \pm b \exp\left(-\frac{\Omega^2}{2}\right). \tag{3}$$

along which the system (1) has folds of maximal torus canards. Moreover, for each fixed $\mathcal{O}(1)$ value of Ω, the system (1) has two maximal torus canards for every value of a in the interval between these fold curves, and none outside the closure of these intervals.

This theorem is also established using geometric desingularisation; however, in this regime, we inflate the circular fold curve along which the attracting and repelling limit cycles meet into a two-torus, rather than the FSN I points. See Sect. 4.

Then, for the high-frequency regime, we establish:

Corollary 1.3 (High-frequency forcing) *Let $\omega = \mathcal{O}(1)$, and let $b = \mathcal{O}(\varepsilon)$. Then, there exists an $\varepsilon_0 > 0$ such that for all $0 < \varepsilon < \varepsilon_0$, there are two curves in the (a, ω) parameter plane given by*

$$a = 1 - \frac{\varepsilon}{8} \pm b \exp\left(-\frac{\omega^2}{2\,\varepsilon}\right). \tag{4}$$

along which the system (1) *has folds of torus canards. Moreover, there exists a pair of torus canards for each parameter value in the interval between these fold curves.*

We note that the presence of torus canards in this type of fast–slow system is signalled by the existence of a fold of limit cycles of the fast system, here at $(x, y) = (1, -\frac{2}{3})$, together with a nearby torus bifurcation in the full system, here at

$$1 - a^2 - \frac{1}{2}\frac{b^2\,\varepsilon^2}{(a^2-1)^2\omega^2 + (\varepsilon - \omega^2)^2} = 0. \tag{5}$$

See "Appendix 1". These two triggering mechanisms arise ubiquitously in fast–slow systems with two or more fast variables.

Having established these theorems for the existence of the primary maximal canards and the torus canards, as well as their folds, we now analyse the relationship between these results. Plainly, the formulas for the curves of folds (2), (3), and (4) in the three different regimes are all representations of the same formula,

$$a = 1 - \frac{\varepsilon}{8} \pm b \exp\left(-\frac{\omega^2}{2\,\varepsilon}\right), \tag{6}$$

in the respective frequency regimes. The exponential term has magnitude b (which is $\mathcal{O}(\sqrt{\varepsilon})$) and is slowly varying with $\overline{\omega}$ in the low-frequency regime (Theorem 1.1), small amplitude ($b = \mathcal{O}(\varepsilon)$) and varying with $\mathcal{O}(1)$ frequency Ω in the intermediate-frequency regime (Theorem 1.2), and exponentially small in ε in the high-frequency regime (Corollary 1.3).

The analysis in all three regions shows that the values of the parameter a for which the canards exist in between the fold curves may similarly be summarised succinctly in one formula:

$$a = 1 - \frac{\varepsilon}{8} - b\cos(\theta_0) \exp\left(-\frac{\omega^2}{2\,\varepsilon}\right). \tag{7}$$

Here, θ_0 is an arbitrary phase, and the magnitude and dynamics of the exponential term are also as discussed above.

It is also of interest to observe that, in the limit of $\omega \to \infty$, formulas (6) and (7) become $a \to a_c := 1 - \frac{\varepsilon}{8}$, which corresponds exactly to the leading order locations of the maximal limit cycle canards in the planar vdP equation, see for example Krupa and Szmolyan (2001). Therefore, as expected, for sufficiently high-frequency forcing, the effect of the forcing averages out to this order, and (1) behaves like the classical planar vdP equation. In this limiting regime, the torus canards of (1) appear to be rotated copies of the limit cycle canards of the planar vdP.

With the above analytical results in hand, we turn next to the results of numerical continuations which confirm that the curves of the folds of primary strong canards observed in the low-frequency regime continue directly to the curves of the folds of torus canards discovered in the intermediate- and high-frequency regimes. This is

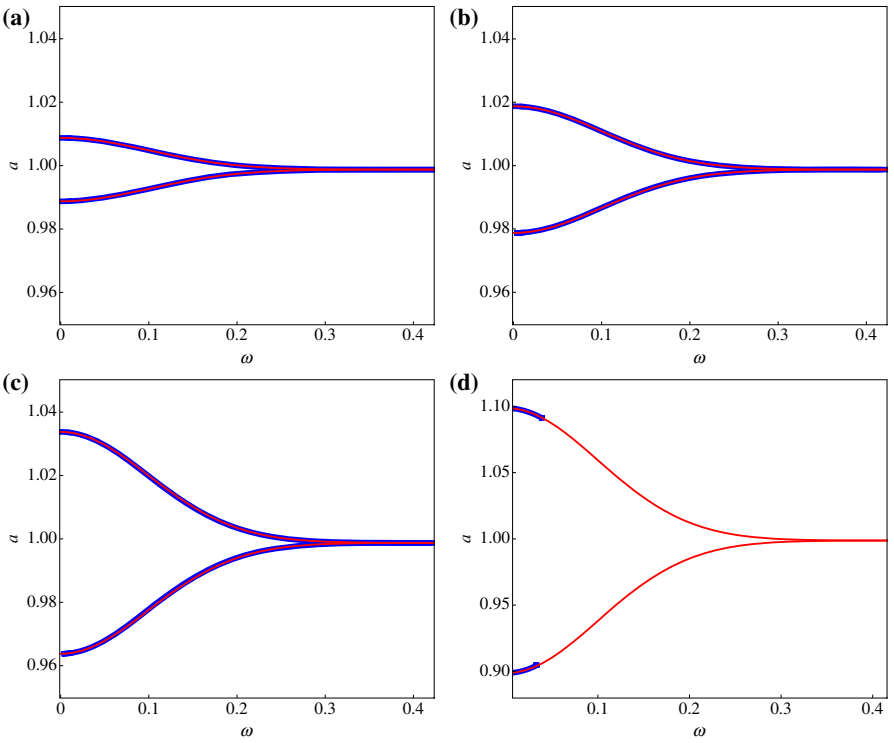

Fig. 2 Curves of folds of maximal canards in the (ω, a) plane as obtained from (6) (*thin red curves*) and two-parameter numerical continuation (*thick blue curves*) for $\varepsilon = 0.01$ and **a** $b = 0.01$; **b** $b = 0.02$; **c** $b = 0.035$l; and **d** $b = 0.1$. For $b = \mathcal{O}(\varepsilon)$ (**a**–**c**), there is good agreement between theoretical (*red*) and numerical (*blue*) results over the entire range of forcing frequencies, including for both the primary maximal canards which exist for $\omega = \mathcal{O}(\varepsilon)$ and the maximal torus canards which exist for $\omega = \mathcal{O}(1)$. Note that the scales in **a**–**c** are the same. For $b = \mathcal{O}(\sqrt{\varepsilon})$ (**d**, in which the vertical scale is different), we find that the numerical continuation terminates when ω is no longer $\mathcal{O}(\varepsilon)$ (Color figure online)

illustrated in Fig. 2, which also shows that the agreement between the formulas and the numerical continuation results is excellent within the parameter regions stated in the theorems. We note that the theory does not appear to extend outside of these regions, and preliminary numerical continuation results reveal different dynamics there. Overall, then, (6) and (7) together with the numerical continuations will directly imply that the primary strong canards, which exist in the low-frequency forcing region, continue naturally to the branches of torus canards, which exist in the high-frequency regime, where the folded singularities cease to exist, with the transition happening in the intermediate-frequency regime. Understanding the continuation dynamics of these curves is one of the main results of this article. Moreover, the results here will help shed light on other models with torus canards. In particular, we observe that numerical simulations of a rotated van der Pol-type model exhibit the same continuation of the maximal canards across the entire range of forcing frequencies, see Figure 5 in Benes et al. (2011). Numerical continuations in other neuronal (or neural) models (Burke et al. 2012) show similar phenomena.

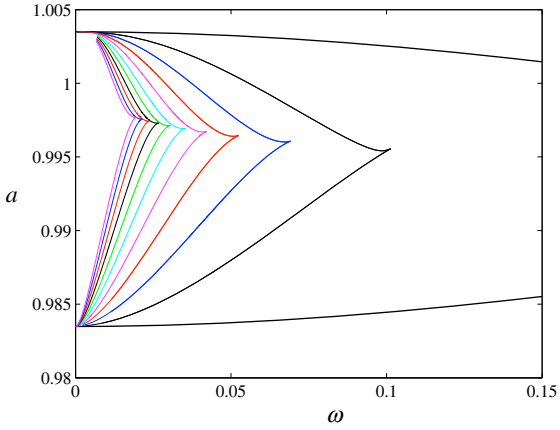

Fig. 3 Curves of folds along the computed branches of primary and secondary canards for $\varepsilon = 0.05$ and $b = 0.01$

In this article, we also study the secondary canards of (1). Secondary canards lie near the primary strong canard for most of their lengths and make a number of small loops around the weak canard, which is also the axis of rotation. We numerically continue the branches of maximal secondary canards of (1) that are created by the folded singularities in the low-frequency regime. In contrast to the primary canards, the secondary canards turn around well before they reach the high-frequency regime, see Fig. 3. Also, we identify the mechanisms which cause the branches to turn. See Sect. 5.

To conclude this article, we demonstrate that (1) serves as a local normal form for slow/fast systems with one slow variable and two fast variables in which the fast subsystem possesses a non-degenerate fold of limit cycles and in which the slow system is subject to time-periodic forcing. These fast–slow systems exhibit torus canard explosions, just as shown here for the fvdP equation (1), and one may therefore directly conclude, by applying the same techniques used herein, that the folds of their canards behave in a similar fashion, see Sect. 6.

Throughout this article, we use the numerical method developed in Desroches et al. (2008, 2010) to find the persistent invariant manifolds and the curves of maximal canards that lie in their intersections. This method, which uses the AUTO continuation software (Doedel et al. 2007), turns the problem of finding the invariant manifolds of slow/fast systems into a boundary value problem for system (1) with the integration time included as a parameter. Then, the parametrised families of solutions of the two-point boundary value problems are continued. This allows to integrate in positive and negative time using pseudo-arclength continuation, approximating the orbit segments of solutions of system (1) subject to particular boundary conditions by orthogonal collocation, which is very well suited to multiple time scale vector fields (see Desroches et al. 2012).

The outline of the article is as follows. In Sect. 2, we consider system (1) with low-frequency forcing, $\omega = \mathcal{O}(\varepsilon)$ and apply canard theory to find the associated primary and secondary canards of folded singularities. In Sect. 3, we prove Theorem 1.1, establishing the existence of the primary maximal canards induced by FSN I points, and

the associated fold curves, including the derivations of (2) and (7) for system (1) in the low-frequency region. We then turn to the cases of intermediate- and high-frequency forcing in Sect. 4, where we study the torus canards of (1). We prove Theorem 1.2 and Corollary 1.3, establishing the existence of the maximal torus canards and their fold curves in these regimes, as given by the formulas (3) and (4). This shows analytically that the curves of folds of the primary maximal canards, which are born in the low-frequency regime, continue for all $\omega > 0$ into the fold curves of the maximal torus canards, as shown in Fig. 4. We also observe that the analytically derived formulas and the curves obtained in the numerical continuations agree over the entire range of forcing frequencies. Then, in Sect. 5, we numerically continue the folds of secondary canards

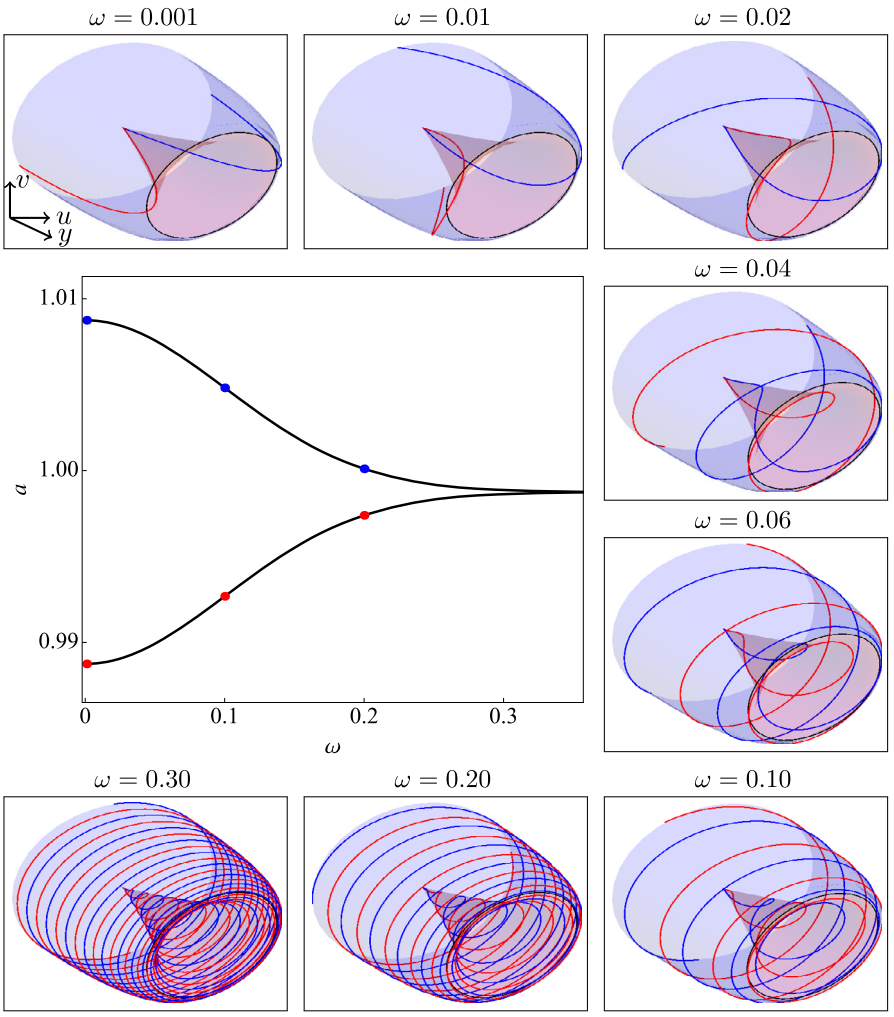

Fig. 4 Two-parameter continuation of folds of primary maximal canards of a folded saddle node (type I) for $\varepsilon = 0.01$ and $b = 0.01$. Orbit segments are plotted in 'Cartesian' coordinates $(u, v, y) = (x\cos\theta, x\sin\theta, y)$

and identify the mechanism by which they turn around well before they reach the high-frequency regime. Also, we analyse how the curves of the folds of secondary canards induced by folded nodes change as the parameter b is varied, up to and including $b = \mathcal{O}(1)$, and hence as the distance between the folded node and the folded saddle is varied. The final main result of this article is presented in Sect. 6. We demonstrate that (1) may be considered as a local normal form for some generic fast–slow systems that have a fold of limit cycles and that undergo a torus canard explosion. In "Appendix 1", we prove, using second-order averaging, the existence of a torus bifurcation in (1) and calculate the locus (5) for this bifurcation in parameter space.

2 Low-Frequency Forcing: Canards of Folded Singularities, Especially of FSN I Points

In this section, we present a brief review and analysis of the folded singularities that system (1) possesses in the regime of low drive frequency, i.e. $\omega = \varepsilon\,\overline{\omega}$, where $\overline{\omega} = \mathcal{O}(1)$ and $0 < \varepsilon \ll 1$. Readers familiar with the theory of folded singularities and their canards may proceed to Sect. 3. In this regime, (1) is

$$\begin{aligned} x' &= y - f(x), \\ y' &= \varepsilon\,(-x + a + b\cos\theta)\,, \\ \theta' &= \varepsilon\,\overline{\omega}. \end{aligned} \tag{8}$$

It is a one-fast/two-slow problem with fast variable x and slow variables (y, θ). We analyse the reduced dynamics associated with (8) and derive the desingularised vector field on the critical manifold. Then, we identify the canards of the folded singularities.

2.1 The Layer and Reduced Systems

Taking the singular limit $\varepsilon \to 0$ in (8), one finds the 1D layer problem

$$x' = y - f(x), \tag{9}$$

where y and θ are parameters. Alternatively, the singular limit $\varepsilon \to 0$ in (1) gives the 2D reduced system

$$\begin{aligned} 0 &= y - f(x), \\ \dot{y} &= -x + a + b\cos\theta, \\ \dot{\theta} &= \overline{\omega}, \end{aligned} \tag{10}$$

where the overdot denotes the derivative with respect to the slow time $t = \varepsilon\,\tau$. The manifolds S_a^ε and S_r^ε are non-unique. Hence, the canards that lie near the manifolds are also non-unique. However, for a fixed choice of invariant manifolds, S_a^ε and S_r^ε, their transverse intersections correspond to maximal canards.

Systems (9) and (10) are two different approximations of the fvdP equation. The idea of geometric singular perturbation theory (GSPT) (Jones 1995) is to combine

information from the 1D layer and 2D reduced problems in order to understand the dynamics of the full 3D fvdP equation for $0 < \varepsilon \ll 1$.

We begin with an analysis of the 1D layer problem (9), which is an approximation of (1) wherein the slow processes are assumed to move so slowly that they are fixed. The *critical manifold* is the set of equilibria of the layer problem (9):

$$S := \left\{(x, y, \theta) \in \mathbb{R}^2 \times \mathbb{S}^1 : y = f(x)\right\}.$$

Linear stability analysis of (9) shows that there are disjoint curves, L, of fold points given by

$$L := \{(x, y, \theta) \in S : x = \pm 1\},$$

which separate the outer attracting sheets, S_a, of S from the middle repelling sheet, S_r, of S. Fenichel theory (Fenichel 1979; Jones 1995) guarantees that the normally hyperbolic segments of S (i.e. the parts of S_a and S_r at $\mathcal{O}(1)$ distances from the fold curve L) will persist as invariant slow manifolds, S_a^ε and S_r^ε, of (1) for $0 < \varepsilon \ll 1$.

The price we pay for the approximation (9) is that we have trivial dynamics on S. To obtain a non-trivial flow on S, we turn to the reduced problem (10), which is an approximation of (1) wherein the fast motions are assumed to be so rapid that they immediately settle to their steady state, which is precisely the critical manifold. In other words, the reduced problem prescribes a non-trivial flow along S. The price we pay for this approximation is that the reduced flow is not defined away from S. Note that the restriction of the flow of (1) to S^ε is a small smooth perturbation of the reduced flow on S.

To analyse the flow on a manifold, we use the coordinates (x, θ). We differentiate the algebraic constraint $y = f(x)$ with respect to t to obtain the evolution equations in this coordinate chart,

$$\begin{aligned}(x^2 - 1)\dot{x} &= -x + a + b\cos\theta,\\ \dot{\theta} &= \overline{\omega}.\end{aligned} \tag{11}$$

The reduced flow (11) is singular along the fold points L of (9). To remove the finite time blow-up of solutions at the folds, we multiply the right-hand side of (11) by $x^2 - 1$ to obtain

$$\begin{aligned}\dot{x} &= -x + a + b\cos\theta,\\ \dot{\theta} &= \overline{\omega}(x^2 - 1),\end{aligned} \tag{12}$$

which is topologically conjugate to (11) under the time rescaling $\mathrm{d}t = (x^2 - 1)\, ds$, and the overdot now denotes derivatives with respect to s. System (12) is equivalent to the reduced flow (11) on the attracting sheets S_a, where the time rescaling $\mathrm{d}t = (x^2 - 1)\,\mathrm{d}s$ preserves the orientation of trajectories. On the repelling sheet S_r, however, we have $x^2 - 1 < 0$, so that the time rescaling reverses the orientation of trajectories. Thus, to obtain the reduced flow (11) on S_r from (12), we simply reverse the direction of trajectories of (12) whenever we are on the repelling sheet of the critical manifold.

2.2 Folded Singularities and Singular Canards

The desingularised system (12) possesses special equilibria called *folded singularities*, M, which are points along the fold curves where the right-hand side of the x-equation vanishes. In system (12), there are infinitely many pairs of such points (when θ is considered in its lift to $\mathbb{R}$):

$$M := \left\{ (x, y, \theta) \in L : \theta = 2k\pi \pm \cos^{-1}\left(\frac{1-a}{b}\right),\ k \in \mathbb{Z} \right\},$$

where $|1-a| \leq b$. Folded singularities are not true equilibria of the reduced flow (11). Instead, they correspond to points of (11) where there is potentially a cancellation of a simple zero in the x-equation and trajectories may pass through the fold (via the folded singularity) with finite speed. Such a trajectory of the reduced flow that passes through a folded singularity and crosses from the attracting (resp. repelling) sheet to the repelling (resp. attracting) sheet is called a *singular canard* (resp. *singular faux canard*) (Szmolyan and Wechselberger 2001; Wechselberger 2005, 2012).

Considered as equilibria of the desingularised system (12), folded singularities are classified according to their linearisation. Folded nodes have real eigenvalues of the same sign. Folded saddles have real eigenvalues of opposite sign, whilst folded foci have complex eigenvalues. In the fvdP equation (1), we find that for $\overline{\omega} > 0$ the folded singularities with

$$\theta_s(k) = 2k\pi - \cos^{-1}\left(\frac{1-a}{b}\right),$$

are folded saddles, whilst the folded singularities with

$$\theta_n(k) = 2k\pi + \cos^{-1}\left(\frac{1-a}{b}\right),$$

are folded nodes provided

$$(1-a)^2 < b^2 < (1-a)^2 + \frac{1}{64\,\overline{\omega}^2}.$$

Folded nodes and folded saddles have been demonstrated to be the organising centres for complex phenomena. Folded nodes for instance have been identified as the cause of the small oscillations in mixed-mode oscillations patterns in various neurophysiological problems (Erchova and McGonigle 2008), such as in a self-coupled FitzHugh–Nagumo model, in a Hodgkin–Huxley model (Rubin and Wechselberger 2008), and in a pituitary lactotroph cell model (Teka et al. 2011). More recently, folded saddles have been identified as playing a significant role in distinguishing between transient spiking and quiescence in a model of propofol anaesthesia (Mitry et al. 2013) and in non-autonomous excitability models (Wechselberger et al. 2014).

2.3 Canards of Folded Saddle-Node Type I Points

Folded nodes and folded saddles can be created through bifurcations in at least two distinct ways in (12): via a folded saddle node (FSN) of type I (Krupa and Wechselberger 2010; Vo and Wechselberger 2015) or via a FSN of type II (Krupa and Wechselberger 2010). Both FSNs correspond to a zero eigenvalue of the folded node (or folded saddle). The two FSN scenarios are distinguished by their geometry. In the FSN I limit, the centre manifold of the FSN I (in system (12)) is tangential to the fold curve. In the FSN II limit, the centre manifold of the FSN II is transverse to the fold curve. We focus here on FSN I and refer to the remark below for FSN II points.

The FSN I is the codimension-1 bifurcation of the desingularised system (12) in which a folded saddle and a folded node coalesce and annihilate each other in a saddle-node bifurcation of folded singularities. For the fvdP equation (1), there are infinitely many such FSN I points: $(x, y, \theta) = (1, -\frac{2}{3}, 2k\pi)$, and they occur for $a = 1 \pm b$ and $\omega = \varepsilon\,\overline{\omega}$. The FSN I at $a = 1 - b$ has its centre manifold on S_r so that the funnel region (enclosed by the strong canard of the folded node / folded saddle canard and the fold curve) vanishes in the FSN I limit. In this case, we expect generic solutions of (1) near this FSN I limit to either be relaxation oscillations or mixed-mode oscillations. The FSN I at $a = 1 + b$ on the other hand has its centre manifold on S_a^+ so that the funnel persists in the FSN I limit and most solutions of (1) can tunnel through S_r and return to S_a. A representative example of the passage through a FSN I bifurcation at $a = 1 + b$ is shown in Fig. 5.

In the FSN limit, the standard folded node/folded saddle theory requires modification. For the FSN I, the following results were recently proved in Vo and Wechselberger (2015), valid for $0 < \varepsilon \ll 1$ and $\mu = \mathcal{O}(\varepsilon^\alpha)$ where $\alpha \geq 1/4$:

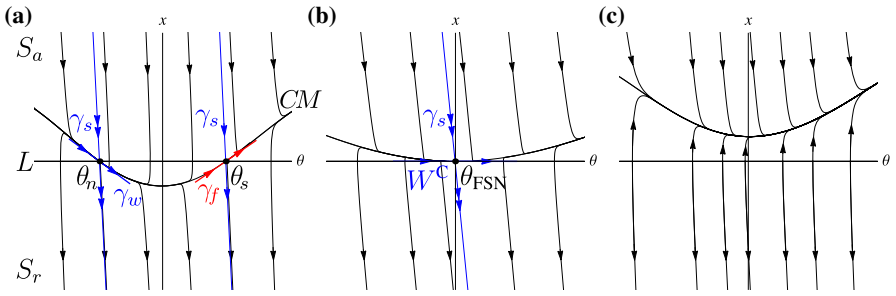

Fig. 5 Reduced flow (11) of the fvdP equation (1) shown in a neighbourhood of the upper fold curve L (defined by $x = 1$, $y = -\frac{2}{3}$) for $\overline{\omega} = 1$, $b = 0.01$, and **a** $a = 1 + \frac{b}{2}$, **b** $a = 1 + b$ and **c** $a = 1 + \frac{3b}{2}$. In **a** where $a < 1 + b$, there is a folded node (θ_n) and a folded saddle (θ_s). The strong and weak eigendirections of the folded node are denoted by γ_s and γ_w, respectively. The singular canard and faux canard of the folded saddle are labelled γ_s and γ_f, respectively. There is a heteroclinic connection CM from θ_n to θ_s, with γ_w tangent to CM at θ_n, and γ_f tangent to CM at θ_s. In **b** where $a = 1 + b$, the folded singularities merge to a FSN I (indicated by θ_{FSN}). In this case, the singular strong canard of the folded node merges with the singular canard of the folded saddle. Meanwhile, the singular weak canard of the folded node merges with the faux canard of the folded saddle to become the centre manifold W^C of the FSN I. In **c** where $a > 1 + b$, the folded singularities (and associated canards) have been destroyed in the FSN I bifurcation, and there are no canard dynamics

1. The singular strong canard of the folded node perturbs to the primary maximal strong canard. The singular canard of the folded saddle perturbs to a maximal canard.
2. There exists a heteroclinic connection CM between the folded nodes and folded saddles of (12). This heteroclinic perturbs to a canard–faux canard solution CM^{ε} that corresponds to both the primary weak canard of the folded node and the faux canard of the folded saddle (faux canards are the equivalent of singular faux canards for $0 < \varepsilon \ll 1$).
3. There exist $\mathcal{O}(\varepsilon^{-1/4})$ canards and faux canards.

Thus, canards and faux canards of the FSN I oscillate about an axis of rotation, which is approximately given by the heteroclinic CM (see Fig. 5a for instance). For the fvdP, we find that $CM := \{(x, y, \theta) \in S : x = a + b\cos\theta\}$. We study the associated maximal canards of (1) in Sect. 3.

Remark 1 For the fvdP equation (1), FSN II points are codimension-2 bifurcation points of the desingularised flow (corresponding to $\overline{\omega} = 0$) and constitute a special case of the FSN I. They can be analysed using the approach presented in Krupa and Wechselberger (2010).

3 Loci of the Maximal Canards for Low Forcing Frequencies

In this section, we analyse system (1) with low-frequency forcing ($\omega = \varepsilon\,\overline{\omega}$). We prove Theorem 1.1, demonstrating that, for $b = \mathcal{O}(\sqrt{\varepsilon})$, formula (2) gives the branches of the folds of the primary maximal canards and that for each value of a in between the fold curves, there are two primary maximal canards of system (1) given in parameter space by (7). More precisely, we analyse the FSN I points to show that formula (2) gives the locus of points at which the primary strong canard of a folded node point merges with the folded saddle maximal canard. We present the analysis for the FSN I that occurs for $a = 1 - b$ and note that the FSN I at $a = 1 + b$ is treated similarly.

For the analysis with low-frequency forcing, we first translate the FSN I at $a = 1-b$ to the origin

$$u = x - 1, \quad v = y + \frac{2}{3}, \quad \eta = a - 1 + b,$$

so that (1) is transformed to

$$\begin{aligned} u' &= v - \left(u^2 + \frac{1}{3}u^3\right), \\ v' &= \varepsilon\left(-u + \eta + b(\cos\theta - 1)\right), \\ \theta' &= \varepsilon\,\overline{\omega}. \end{aligned} \tag{13}$$

We then inflate the FSN I singularity to a hypersphere using the spherical blow-up transformation:

$$u = \overline{r}^2\overline{u}, \quad v = \overline{r}^4\overline{v}, \quad \theta = \overline{r}\overline{\theta}, \quad \varepsilon = \overline{r}^4\overline{\varepsilon},$$

where $\overline{u}^2 + \overline{v}^2 + \overline{\theta}^2 + \overline{\varepsilon}^2 = 1$. Moreover, we rescale the parameters b and η as

$$b = \sqrt{\varepsilon}\beta, \quad \eta = \varepsilon\,\gamma,$$

where $\beta = \mathcal{O}(1)$ and $\gamma = \mathcal{O}(1)$. Also, we append the trivial equation $\varepsilon' = 0$ to system (13) and take $\mu > 0$ sufficiently small. The (spherical) blow-up transformation is a map from $B := \mathbb{S}^3 \times [-\mu, \mu]$ into $\mathbb{R}^4$. We examine the vector fields induced by this coordinate transformation in two useful coordinate charts: the entry-exit chart (or phase-directional chart) $K_1 : \{\overline{v} = 1\}$ and the rescaling (or central) chart $K_2 : \{\overline{\varepsilon} = 1\}$, beginning with K_1.

In chart K_1, the blow-up coordinates are

$$u = r_1^2 u_1, \quad v = r_1^4, \quad \theta = r_1\theta_1, \quad \varepsilon = r_1^4\,\varepsilon_1, \tag{14}$$

where the subscript corresponds to the chart number. The governing equations are

$$\begin{aligned}
\dot{u}_1 &= 1 - u_1^2 - \frac{1}{3}r_1^2 u_1^3 - \frac{1}{2}\,\varepsilon_1\,u_1 F,\\
\dot{r}_1 &= \frac{1}{4}r_1\,\varepsilon_1\,F,\\
\dot{\theta}_1 &= r_1\,\varepsilon_1\,\overline{\omega} - \frac{1}{4}\,\varepsilon_1\,\theta_1 F,\\
\dot{\varepsilon}_1 &= -\,\varepsilon_1^2\,F,
\end{aligned} \tag{15}$$

where $F(u_1, \theta_1, r_1) = -u_1 + r_1^2\,\varepsilon_1\,\gamma + \beta\sqrt{\varepsilon_1}\,(\cos(r_1\theta_1) - 1)$, we have desingularised the vector field by a factor of r_1^2, and the overdot denotes the derivative with respect to the new time. The hyperplanes $\{r_1 = 0\}$ and $\{\varepsilon_1 = 0\}$ are invariant. In the invariant subspace $\{r_1 = 0\}$, $\theta_1 = 0$ is an attracting fixed point. The line

$$\ell_u = \{(u_1, r_1, \theta_1, \varepsilon_1) = (u_1, 0, 0, 0)\}$$

is invariant, and on it the system dynamics are governed by $\dot{u}_1 = 1 - u_1^2$. Furthermore, on ℓ_u there are attracting and repelling fixed points $p_a = (1, 0, 0, 0)$ and $p_r = (-1, 0, 0, 0)$, which, respectively, have centre manifolds $N_{a,1}$ and $N_{r,1}$ in the half space $\varepsilon_1 > 0$.

In order to demonstrate the existence of the primary maximal canards, we will show that there is a heteroclinic connection between p_a and p_r in the hyperplane $\{r_1 = 0\}$ and that this heteroclinic orbit persists for sufficiently small values of r_1, using Melnikov theory. The persistent connections correspond to the primary maximal canards. We carry out the relevant analysis in the rescaling chart K_2, where the blow-up transformation is given by

$$u = r_2^2 u_2, \quad v = r_2^4 v_2, \quad \theta = r_2\theta_2, \quad \varepsilon = r_2^4. \tag{16}$$

Note that $r_2 = \varepsilon^{1/4}$, so that chart K_2 corresponds to an ε-dependent rescaling of the fvdP equation. Also, the coordinates in the two charts are related via the following transformation:

$$r_2 = r_1\,\varepsilon_1^{1/4}, \quad u_2 = u_1\,\varepsilon_1^{-1/2}, \quad v_2 = \varepsilon_1^{-1}, \quad \theta_2 = \theta_1\,\varepsilon_1^{-1/4},$$

where $\varepsilon_1 > 0$.

In chart K_2, the blown-up system (13) is

$$\begin{aligned} \dot{u}_2 &= v_2 - u_2^2 - \frac{1}{3} r_2^2 u_2^3, \\ \dot{v}_2 &= -u_2 + r_2^2 \gamma + \beta\,(\cos(r_2\theta_2) - 1)\,, \\ \dot{\theta}_2 &= r_2\,\overline{\omega}, \end{aligned} \tag{17}$$

where we have desingularised the vector field (i.e. rescaled by r_2^2) and the overdot denotes the derivative with respect to the new time t_2. This system is singularly perturbed with fast variables (u_2, v_2) and slow variable θ_2. Rewriting the blown-up system in non-autonomous form, we have

$$\begin{aligned} \dot{u}_2 &= v_2 - u_2^2 - \frac{1}{3} r_2^2 u_2^3, \\ \dot{v}_2 &= -u_2 + r_2^2 \gamma + \beta \left(\cos(r_2^2\overline{\omega}t_2)\cos(r_2\theta_{2,0}) - 1\right) - \beta \sin(r_2^2\overline{\omega}t_2)\sin(r_2\theta_{2,0}), \end{aligned} \tag{18}$$

where $\theta_{2,0}$ is an arbitrary phase. For $\overline{\omega}$ and t_2 of $\mathcal{O}(1)$, we have

$$\begin{aligned} \cos(r_2^2\overline{\omega}t_2)\cos(r_2\theta_{2,0}) - 1 &= \mathcal{O}(r_2^2) \text{ as } r_2 \to 0, \\ \sin(r_2^2\overline{\omega}t_2)\sin(r_2\theta_{2,0}) &= \mathcal{O}(r_2^3) \text{ as } r_2 \to 0. \end{aligned}$$

The unperturbed problem corresponding to (18) is obtained by setting $r_2 = 0$,

$$\begin{aligned} u_2' &= v_2 - u_2^2, \\ v_2' &= -u_2. \end{aligned} \tag{19}$$

This system is Hamiltonian with Hamiltonian function

$$H(u_2, v_2) = \mathrm{e}^{-2v_2}\left(u_2^2 - v_2 - \frac{1}{2}\right),$$

and non-canonical formulation

$$\begin{aligned} \dot{u}_2 &= \frac{1}{2}\mathrm{e}^{2v_2}\frac{\partial H}{\partial v_2}, \\ \dot{v}_2 &= -\frac{1}{2}\mathrm{e}^{2v_2}\frac{\partial H}{\partial u_2}. \end{aligned}$$

The level curves of H are presented in Fig. 6. The contour Γ separates closed trajectories from unbounded orbits and has the explicit time parametrisation

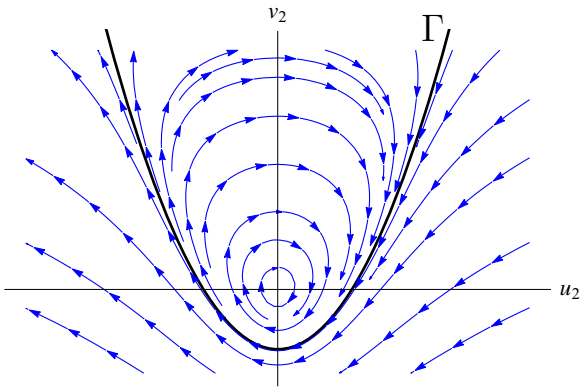

Fig. 6 Contours of the Hamiltonian function H. Periodic solutions of (19) correspond to level sets with $-\frac{1}{2} \leq H < 0$. Unbounded solutions of (19) correspond to $H > 0$. The $H = 0$ contour, Γ, is the heteroclinic connecting the points p_a and p_r at infinity

$$(u_{2,\Gamma}, v_{2,\Gamma}) = \left(-\frac{1}{2}t_2, \frac{1}{4}t_2^2 - \frac{1}{2}\right).$$

The separatrix Γ corresponds to the singular strong canard of the FSN I. In geometric terms, it is a heteroclinic orbit that lies on the upper hemisphere and connects the fixed points p_a and p_r, both of which lie on the equator of the blown-up sphere.

We now use the Melnikov method to analyse the persistence of Γ under small-amplitude perturbations. As applied to (18), Melnikov theory measures the splitting distance D between the curves of solutions of the perturbed system that are forward and backward asymptotic to p_r and p_a, respectively. We develop D in an asymptotic series in the small parameter r_2:

$$D(r_2) = d_1 r_2^2 + d_2 r_2^3 + \cdots,$$

where the terms in the Melnikov integral are given by

$$d_1 = \int_{-\infty}^{\infty} \nabla H|_\Gamma \cdot \begin{pmatrix} -\frac{1}{3}u_{2,\Gamma}^3 \\ \gamma + \frac{\beta}{r_2^2}\left(\cos(r_2^2\overline{\omega}t_2)\cos(r_2\theta_{2,0}) - 1\right) \end{pmatrix} \mathrm{d}t_2,$$

$$d_2 = \int_{-\infty}^{\infty} \nabla H|_\Gamma \cdot \begin{pmatrix} 0 \\ -\frac{\beta}{r_2^3}\sin(r_2^2\overline{\omega}t_2)\sin(r_2\theta_{2,0}) \end{pmatrix} \mathrm{d}t_2.$$

We note that the integrand in d_2 is an odd function of t_2 so the integral evaluates to zero and the sine term has no contribution to the distance measurement D. We also note that the $\frac{\cos(r_2^2\overline{\omega}t_2)\cos(r_2\theta_{2,0})-1}{r_2^2}$ term in d_1 is $\mathcal{O}(1)$ with respect to r_2. The integral d_1 was evaluated by taking $\cos z = \mathrm{Re}(\mathrm{e}^{iz})$, completing the square in the exponential, and deforming the contour in the complex plane. The result is

$$d_1 = \frac{e\sqrt{2\pi}}{r_2^2}\left\{\beta - r_2^2\left(\frac{1}{8} + \gamma\right) - \beta \mathrm{e}^{-\frac{1}{2}r_2^4\overline{\omega}^2}\cos(r_2\theta_{2,0})\right\}.$$

Substituting this into the bifurcation equation $D = 0$, we have

$$r_2^2\left(\frac{1}{8}+\gamma\right)+\beta\cos(r_2\theta_{2,0})\left(\mathrm{e}^{-\frac{1}{2}r_2^4\overline{\omega}^2}-1\right)=0.$$

Thus, reverting to a, b, ε, and $\overline{\omega}$, the primary maximal canards for the FSN I are given by

$$a = 1-\frac{\varepsilon}{8}-b\cos(\theta_0)\exp\left(-\frac{\varepsilon\,\overline{\omega}^2}{2}\right), \tag{20}$$

which is (7). We remark that θ_0 is the arbitrary phase $\theta_{2,0}$ in the original θ coordinate (i.e. $\theta_0 = r_2\theta_{2,0}$). This completes the demonstration that (7) holds for low-frequency forcing, giving the locus of points at which the primary maximal canards exist. Moreover, one also sees that, for each $\overline{\omega}$, the folds of the primary maximal canards at the endpoints of these parameter intervals are given by

$$a = 1-\frac{\varepsilon}{8}\pm b\exp\left(-\frac{\varepsilon\,\overline{\omega}^2}{2}\right), \tag{21}$$

which is precisely (2). The loci in the $(\overline{\omega}, a)$ plane of the folds of maximal canards mark the upper and lower boundaries of the regime in which the primary maximal canards exist. This completes the proof of Theorem 1.1.

Remark 2 For $\omega = \varepsilon\,\overline{\omega}$, one may extend the result of Theorem 1.1 to the parameter regime in which $b = \mathcal{O}(\varepsilon^{\frac{1}{4}})$. Let $b = \varepsilon^{\frac{1}{4}}\,\beta$ and $\eta = \varepsilon^{\frac{3}{4}}\,\gamma$, where β and γ are $\mathcal{O}(1)$ with respect to ε. Then, the perturbation terms in the v_2 component of the non-autonomous system become:

$$r_2\left[\gamma+\frac{\beta}{r_2^2}\left(\cos(r_2^2\overline{\omega}t_2)\cos(r_2\theta_{2,0})-1\right)-\frac{\beta}{r_2^2}\sin(r_2^2\overline{\omega}t_2)\sin(r_2\theta_{2,0})\right].$$

Here, the even terms are $\mathcal{O}(r_2)$ as $r_2 \to 0$, so that one may proceed with a similar Melnikov calculation as above, and the odd terms again do not contribute to leading order in the Melnikov calculation.

We further note that a blow-up and Melnikov computation similar to that just presented for the FSN I points may be done for the folded nodes and folded saddles, and this gives the location of the maximal canards as

$$\theta_{n,s}(k)\approx 2k\pi\pm\cos^{-1}\left(\frac{1-a-\varepsilon/8}{b}+\mathcal{O}(b)\right),\qquad k\in\mathbb{Z}.$$

See also equation (42) in Benes et al. (2011).

We further remark that our analysis here identifies the existence of a fold of canard solutions and then explicitly tracks that special maximal canard solution in the (ω, a) plane. The analysis in Vo and Wechselberger (2015) on the other hand deals with the existence of primary and secondary canards (and the associated bifurcation delay) as

the system transitions from a folded node regime to a folded saddle regime via the FSN I bifurcation. The analysis presented herein should carry over to the general FSN I case in Vo and Wechselberger (2015).

4 Loci of the Torus Canards and Their Folds for Intermediate- and High-Frequency Forcing

In this section, we study system (1) in the intermediate-frequency regime with $\omega = \sqrt{\varepsilon}\Omega$ and $\Omega = \mathcal{O}(1)$, as well as in the high-frequency regime with $\omega = \mathcal{O}(1)$. We prove Theorem 1.2, demonstrating that (1) possesses a family of torus canards in the intermediate-frequency regime, in between the twofold curves (3) of these torus canards. The central methods used in the proof are geometric desingularisation—in which we use a cylindrical blow-up of the fold curve rather than a spherical blow-up as used in the previous section—and a Melnikov calculation to identify the parameter values for which the torus canards exist. After Theorem 1.2 is established, we prove Corollary 1.3 for the high-frequency regime.

In the intermediate-frequency regime, system (1) is equivalent to

$$\begin{aligned} x' &= y - f(x), \\ y' &= \varepsilon(-x + a + b\cos\theta), \\ \theta' &= \sqrt{\varepsilon}\Omega. \end{aligned} \tag{22}$$

First, we rectify the fold curve so that it coincides with the θ axis,

$$u = x - 1, \quad v = y + \frac{2}{3}, \quad \alpha = a - 1.$$

Also, we recall

$$\alpha = \varepsilon\,\tilde{\alpha}, \quad b = \varepsilon\,\tilde{\beta},$$

where $\tilde{\alpha}$ and $\tilde{\beta}$ are $\mathcal{O}(1)$ with respect to ε. This transforms (22) to the following system:

$$\begin{aligned} u' &= v - u^2 - \frac{1}{3}u^3, \\ v' &= -\varepsilon\, u + \varepsilon^2(\tilde{\alpha} + \tilde{\beta}\cos\theta), \\ \theta' &= \sqrt{\varepsilon}\Omega. \end{aligned} \tag{23}$$

Next, we perform the following cylindrical blow-up transformation:

$$u = \overline{r}\overline{u}, \quad v = \overline{r}^2\overline{v}, \quad \varepsilon = \overline{r}^2\overline{\varepsilon}, \tag{24}$$

which transforms the circle of fold points into a torus (this contrasts with the spherical blow-up of the FSN I point in the previous section). Append the trivial equation $\varepsilon' = 0$ to system (23) and let $\mu > 0$ be sufficiently small. For each $\theta \in \mathbb{S}^1$ and

for all non-negative values of the system parameters, the coordinate change is a map from $B := \mathbb{S}^2 \times [-\mu, \mu]$ into $\mathbb{R}^3$. We examine the vector fields induced by (23) in the entry-exit (or phase-directional) chart $K_1 = \{\overline{v} = 1\}$ and the rescaling chart $K_2 = \{\overline{\varepsilon} = 1\}$.

In chart K_1, the coordinates are

$$u = r_1 u_1, \quad v = r_1^2, \quad \varepsilon = r_1^2 \varepsilon_1 .$$

Setting $F(u_1, r_1, \varepsilon_1, \theta, \tilde{\alpha}, \tilde{\beta}) = -u_1 + \varepsilon_1 r_1(\tilde{\alpha} + \tilde{\beta}\cos(\theta))$, we find that the system in chart K_1 is

$$\begin{aligned} \dot{u}_1 &= 1 - u_1^2 - \frac{1}{3} r_1 u_1^3 - \frac{u_1 \varepsilon_1}{2} F, \\ \dot{r}_1 &= \frac{r_1 \varepsilon_1}{2} F, \\ \dot{\theta} &= \sqrt{\varepsilon_1}\Omega, \\ \dot{\varepsilon}_1 &= -\varepsilon_1^2 F, \end{aligned} \tag{25}$$

where we have desingularised the vector field by rescaling the time variable by a factor of r_1 and the overdot denotes derivatives with respect to the new time variable. In the phase space of (25), the hyperplanes $\{r_1 = 0\}$ and $\{\varepsilon_1 = 0\}$ are invariant. In addition, for every $(\tilde{\alpha}, \tilde{\beta})$, there is an invariant line

$$\ell_u = \{(u_1, r_1, \varepsilon_1) = (u_1, 0, 0)\}$$

on which the dynamics are governed by $\dot{u}_1 = 1 - u_1^2$ and $\dot{\theta} = 0$. Moreover, for every $(\tilde{\alpha}, \tilde{\beta})$, the points

$$p_a = (1, 0, 0) \quad \text{and} \quad p_r = (-1, 0, 0)$$

are attracting and repelling fixed points, respectively, on ℓ_u, and they have two-dimensional centre manifolds $N_{a,1}$ and $N_{r,1}$ in the half space $\varepsilon_1 > 0$.

Having established the dynamics in chart K_1, we now analytically continue solutions in chart K_1 into chart K_2 in order to understand the geometric structures in K_2 and their connections. In chart K_2, the coordinates are

$$u = r_2 u_2, \quad v = r_2^2 v_2, \quad \varepsilon = r_2^2, \tag{26}$$

and these coordinates are related to those of chart K_1 via the following coordinate transformation:

$$u_2 = u_1 \varepsilon_1^{-1/2}, \quad v_2 = \varepsilon_1^{-1}, \quad r_2 = r_1 \varepsilon_1^{1/2},$$

where $\varepsilon_1 > 0$.

In chart K_2, the system is

$$\begin{aligned} \dot{u}_2 &= v_2 - u_2^2 - \frac{1}{3} r_2 u_2^3, \\ \dot{v}_2 &= -u_2 + r_2 \left(\tilde{\alpha} + \tilde{\beta} \cos(\Omega t_2 + \theta_0) \right), \end{aligned} \tag{27}$$

where we have rescaled time by a factor of r_2 to desingularise the vector field (with t_2 denoting this rescaled time variable), the overdot denotes the derivative with respect to t_2, and we have written the system as a non-autonomous system. For reference, we emphasise the relation $\sqrt{\varepsilon} = r_2$. We now show that system (27) possesses a special family of homoclinic orbits, connecting the point at infinity to itself, which implies that the orbits connect the points p_r and p_a identified in chart K_1. These orbits correspond to singular torus canards of the original system (22).

The unperturbed problem associated with system (27) is given by

$$\begin{aligned} \dot{u}_2 &= v_2 - u_2^2, \\ \dot{v}_2 &= -u_2, \end{aligned}$$

which is the same as (19). As shown in the previous section, this unperturbed system is Hamiltonian

$$H(u_2, v_2) = \mathrm{e}^{-2v_2} \left(u_2^2 - v_2 - \frac{1}{2} \right).$$

Along the level set $\Gamma := \{H = 0\}$, which is the separatrix between bounded and unbounded solutions (see Fig. 6), the solutions are given explicitly by

$$u_{2,\Gamma}(t_2) = -\frac{t_2}{2}, \qquad v_{2,\Gamma}(t_2) = \frac{t_2^2}{4} - \frac{1}{2}.$$

In the language of dynamical systems, it is a homoclinic orbit to infinity.

With the above information about the unperturbed system in hand, we now show that Γ persists for sufficiently small r_2 in (27). We use a straightforward generalisation of Proposition 3.5 of Krupa and Szmolyan (2001), where we note that the perturbation terms there are strictly autonomous, whereas here the perturbation terms include a small-amplitude, time-periodic function, and a compactification of the phase space can be used. Moreover, we observe that the parameter there, λ_2, is also treated as being a small variable via the linear scaling of λ with r_2, whereas here we have chosen instead to scale the parameters α and b with ε from the outset and to treat $\tilde{\alpha}, \tilde{\beta} = \mathcal{O}(1)$ as parameters. In this manner, r_2 is the only small variable in the analysis here.

The splitting distance between the manifolds $N_{a,2}$ and $N_{r,2}$ for system (27) is

$$D(r_2) = d_{r_2} r_2 + \cdots .$$

Here, the dependence of the Melnikov function on the system parameters is implicit. We find

$$d_{r_2} = \int_{-\infty}^{\infty} \nabla H|_{\Gamma} \cdot \begin{pmatrix} -\frac{1}{3}u_{2,\Gamma}^3 \\ \tilde{\alpha} + \tilde{\beta}\cos(\Omega t_2 + \theta_0) \end{pmatrix} \mathrm{d}t_2$$
$$= -\frac{e}{2}\sqrt{2\pi}\left(\frac{1}{8} + \tilde{\alpha} + \tilde{\beta}\mathrm{e}^{-\frac{\Omega^2}{2}}\cos(\theta_0)\right), \tag{28}$$

where the last term in the integral was evaluated by using $\cos(z) = \mathrm{Re}(\mathrm{e}^{iz})$, completing the square on the exponential, and shifting the contour in the complex plane. Hence, reverting to the given parameters, we see that to leading order the splitting distance is

$$D = -\frac{e}{2}\sqrt{2\pi}\left[\frac{\sqrt{\varepsilon}}{8} + \frac{a-1}{\sqrt{\varepsilon}} + \frac{b}{\sqrt{\varepsilon}}\mathrm{e}^{-\frac{\Omega^2}{2}}\cos(\theta_0)\right]. \tag{29}$$

Therefore, for each b satisfying the hypotheses of the theorem and for ε small enough, the simple zeroes of the Melnikov function are given in the (a, Ω) plane by

$$a = 1 - \frac{\varepsilon}{8} - b\mathrm{e}^{-\frac{\Omega^2}{2}}\cos(\theta_0). \tag{30}$$

This formula, which is exactly (7) in the intermediate-frequency regime, gives the parameter values for which system (27) has a one-parameter (θ_0) family of persistent homoclinic orbits, and these persistent homoclinic orbits of (27) are the torus canards of (22).

Also, as a direct corollary, we observe that the envelope of the family of torus canards is given by

$$a = 1 - \frac{\varepsilon}{8} \pm b\exp\left(-\frac{\Omega^2}{2}\right), \tag{31}$$

which is precisely formula (3). This completes the proof of Theorem 1.2.

To conclude this section, we prove Corollary 1.3. The proof follows by extending, in a straightforward manner, the above analysis of the persistent homoclinics and the folds of the torus canards in the proof of Theorem 1.2 for the intermediate-frequency forcing regime to the high-frequency forcing regime. In particular, in the high-frequency regime, $\omega = \mathcal{O}(1)$, which corresponds to taking $\Omega = \mathcal{O}(1/\sqrt{\varepsilon})$ in the above analysis. Following exactly along the above calculations, the geometric desingularisation method yields the same equation (27) in chart K_2, but now the small-amplitude time-periodic forcing term has high-frequency $\Omega = \mathcal{O}(1/\sqrt{\varepsilon})$. Hence, the suitable version of the Melnikov theory is that for rapidly forced systems, and the splitting distance along Γ is again given by (31), which is now exponentially small in ε, since $\Omega = \mathcal{O}(1/\sqrt{\varepsilon})$. The system here fits into the framework of rapidly forced Hamiltonian systems studied in Gelfreich (1997), and we have verified that the hypotheses of Gelfreich (1997) are satisfied for our problem, once the vector field has been compactified. Consequently, the result carries over by Theorem 1 of Gelfreich (1997), which states that the splitting distance is given to leading order by the Melnikov function; see also Delshams and Seara (1992) and Delshams and Seara (1997) for the analysis of the splitting distance in time-periodically perturbed planar Hamiltonian systems. This completes the proof of Corollary 1.3.

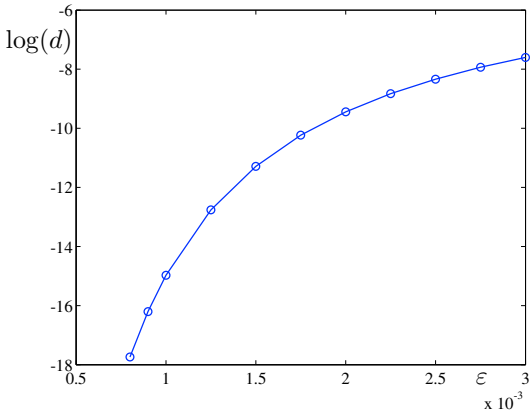

Fig. 7 Width of the canard region in the $\omega = O(1)$ regime, as a function of ε for $b = 0.01$

The result of this Corollary for the high-frequency regime also agrees well with the results obtained from numerical simulations. In Fig. 7, for $\omega = O(1)$, we present a computation of the distance between the twofold of maximal primary canards as a function of ε. We gathered the control points obtained for various computations for eleven fixed values of ε, decreasing from $3 \cdot 10^{-3}$ down to $8 \cdot 10^{-4}$ and plotted them on a logarithmic scale. The hyperbolic shape of the resulting curve confirms that this distance is exponentially small in ε as ε tends to 0.

5 Secondary Canards

Having established the existence of the primary strong canards and their folds, we now turn our attention to the secondary canards of the folded nodes of (1), which exist in the low-frequency forcing regime $\omega = \varepsilon\,\overline{\omega}$. By definition, secondary canards lie in the transverse intersections of the invariant slow manifolds S_a^ε and S_r^ε. A representative example of these manifolds and their intersections (i.e. the secondary canards) is shown in Fig. 8. These manifolds are computed from curves of initial conditions traced on the attracting and repelling sheets, respectively, of the critical manifold S, up to a cross section at fixed angle θ corresponding to the maximal torus canard (Desroches et al. 2008, 2010):

$$\Sigma_n = \left\{ \theta_n = \cos^{-1}\left(\frac{1 - a - \varepsilon/8}{b} + \mathcal{O}(b) \right) \right\}.$$

In Sect. 5.1, we study the folds of the secondary canards and investigate how they change in the (ω, a) plane under variation of the forcing amplitude b (analogous to the folds of the primary canards). We then investigate in Sect. 5.2 how large-amplitude oscillations can grow from small-amplitude oscillations.

5.1 Continuation of Secondary Canards

As shown in Fig. 8, the invariant slow manifolds $S_a^\varepsilon \cap \Sigma_n$ and $S_r^\varepsilon \cap \Sigma_n$ spiral around one another, which is typical of a folded node. More precisely, let $\mu := \lambda_w/\lambda_s$,

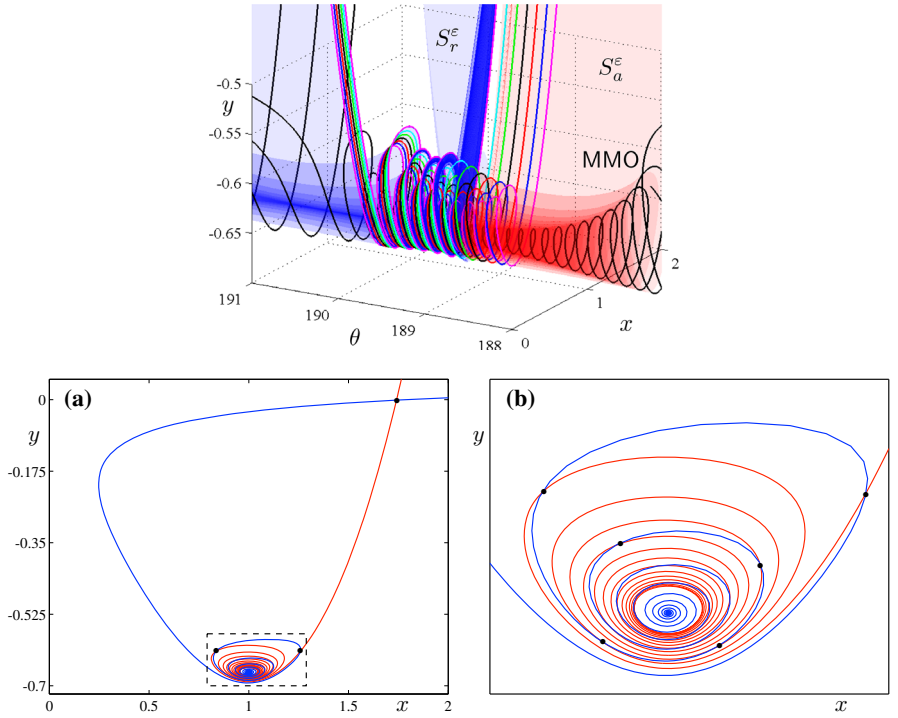

Fig. 8 Attracting (S_a^ε, *red*) and repelling (S_r^ε, *blue*) slow manifolds of system (1) for $a = 0.9935$, $b = 0.01$, $\omega = 0.005$, and $\varepsilon = 0.05$, together with a stable mixed-mode oscillation consisting of one large-amplitude oscillation and six small-amplitude oscillations found for the same parameter values by direct simulation. Bottom row: invariant slow manifolds S_a^ε (*red*) and S_r^ε (*blue*) of system (1) in the cross section Σ_n. The secondary canards are identified as the intersections (*black dots*) of S_a^ε and S_r^ε (Color figure online)

$|\lambda_w| < |\lambda_s|$, denote the eigenvalue ratio of a folded node, regarded as an equilibrium of the desingularised system (12). Provided ε is sufficiently small and μ is bounded away from zero, the total number of (primary and secondary) maximal canards is $s_{\max} + 1$, where

$$s_{\max} = \left\lfloor \frac{\mu + 1}{2\mu} \right\rfloor,$$

and $\lfloor \cdot \rfloor$ denotes the floor function. In particular, a persistent branch of secondary canards bifurcates from the weak canard in a transcritical bifurcation for odd integer values of μ^{-1} (Wechselberger 2005).

Remark 3 The kth secondary canard exhibits k small oscillations about the weak canard for $k = 1, 2, \ldots, s_{\max} - 1$. These small oscillations are localised to an $\mathcal{O}(\sqrt{\varepsilon})$ neighbourhood of the folded node (Wechselberger 2005, 2012). Moreover, trajectories on S_a^ε situated between γ_{k-1} and γ_k, $k = 1, 2, \ldots, s_{\max}$ execute k small oscillations about the weak canard, where γ_0 and $\gamma_{s_{\max}}$ correspond to the primary strong canard and primary weak canard, respectively.

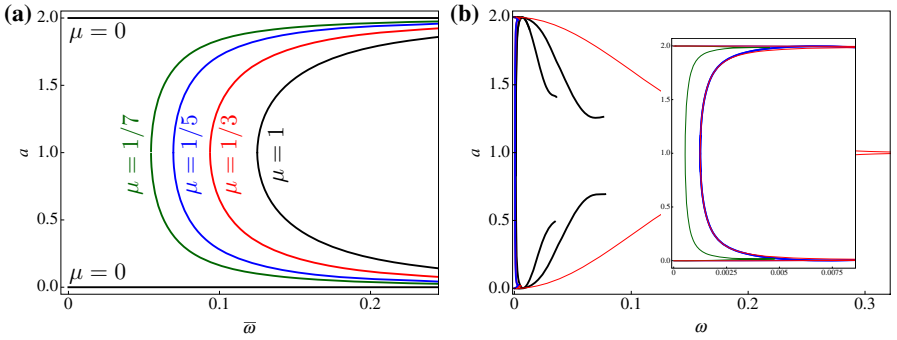

Fig. 9 Resonance curves for $b = 1$, and **a** $\varepsilon = 0$ and **b** $\varepsilon = 0.01$. In **b**, the theoretically computed curve of maximal canards for the FSN I (2) is shown in *red* (*thin outer curve*). Inside this envelope, there are *two black resonance curves*. Both correspond to the numerical continuation of folds of maximal canards. The outermost black curve corresponds to the FSN I (i.e. where $\mu = 0$). Note that (2) breaks down when ω is no longer $\mathcal{O}(\varepsilon)$. The *inner black curve* corresponds to the maximal canard of the degenerate folded node (i.e. where $\mu = 1$). The *inset* shows the numerical continuation of the folds of canards corresponding to $\mu = 1$ and $\mu = 1/3$. In particular, for the $\mu = 1$ resonance, we compare the numerically computed result (*blue*) and the theoretical result obtained in (32) (*red*) and find that there is excellent agreement away from the FSN I boundaries (Color figure online)

By tracking the resonances $\mu^{-1} = 2k + 1, k = 0, 1, 2, \ldots$, we can follow (in the singular limit) the locations in the $(\overline{\omega}, a)$ plane where the secondary canards are born. Figure 9 shows an example for $b = 1$. The non-singular (ω, a) plane shows that only the folds of canards corresponding to the FSN I and the degenerate folded node extend into the intermediate-frequency regime. All other branches of folds of canards are restricted to the low-frequency regime $\omega = \mathcal{O}(\varepsilon)$.

Remark 4 Note that the resonance curves in Fig. 9 bear no resemblance to the curves of folds of secondary canards in Fig. 3. This is to be expected since $b = \mathcal{O}(\sqrt{\varepsilon})$ in Fig. 3, which implies that $\mu = \mathcal{O}(\sqrt{\varepsilon})$ and the folded node theory does not apply.

For the degenerate node ($\mu = 1$), a Melnikov computation similar to that in Sects. 3 and 4 shows that the locus of the primary maximal canard of the degenerate folded node in the $(\overline{\omega}, a)$ plane is

$$a = 1 - \frac{\varepsilon}{8} \pm \sqrt{b^2 - \frac{1}{64\overline{\omega}^2}} \exp\left(-\frac{1}{2}\,\varepsilon\,\overline{\omega}^2\right), \tag{32}$$

which holds provided $\overline{\omega} = \mathcal{O}(1)$, $\sqrt{b^2 - \frac{1}{64\overline{\omega}^2}} = \mathcal{O}(\varepsilon)$ and $\sqrt{b^2 - (1-a)^2} = \mathcal{O}(\sqrt{\varepsilon})$. The inset of Fig. 9 shows that there is excellent agreement between this theoretically computed curve and the curve obtained from numerical continuation. The deviation between theoretical and numerical results for this degenerate folded node maximal canard starts to become significant when the degenerate node branches approach the FSN I branches. We note an important implication: all secondary canards due to folded nodes are restricted to the region of the (ω, a) plane bounded by $\omega = 0$, the locus of the folds of maximal canards of the FSN I and the locus of the maximal canards of the degenerate folded node.

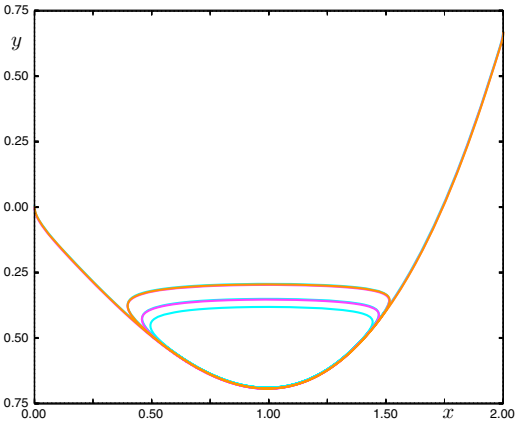

Fig. 10 Projection of the one-loop (*outer orange*), two-loop (*central magenta*), and three-loop (*inner cyan*) secondary canards of (1) shown for $\omega = 0.01$, $\varepsilon = 0.01$, $b = 0.01$, and $a = 1.0034909031$ (one-loop), $a = 1.0034909029$ (two-loop), and $a = 1.0034909029$ (three-loop) shown in the (x, y) plane (Color figure online)

As was the case for the numerical continuation of the folds of the primary canards and the folds of the torus canards, the numerical continuation of the maximal secondary canards is done by solving families of boundary value problems and computing branches of such solutions using pseudo-arclength continuation. Along these branches, a number of fold points can be detected, and then the curves of folds of secondary canards can be continued in two parameters. For a representative set of parameter values, the folds of the first, second, . . ., tenth secondary canards (i.e. with respectively one, two, . . ., ten loops) are shown in the (ω, a) plane in Fig. 3. The outermost envelope in Fig. 3 is the curves of folds of primary canards. The rightmost path enclosed by the fold curve of the primary strong canards represents the fold curve of the first (one-loop) secondary canard, and each successive curve to the left represents a family of folds of secondary canards with one additional loop. These branches of folds of secondary canards emanate from the FSN I points at $a = 1 - \frac{\varepsilon}{8} \pm b$. As ω is increased, the corresponding pairs of n-loop branches come together at turning points.

It is also useful to examine projections of the secondary canards onto the (x, y) plane. In Fig. 10, we show the first three maximal secondary canards, with respectively, one loop (yellow), two loops (red), and three loops (blue). The highest loops of the 2-loop and 3-loop maximal secondary canards are observed to lie extremely close to the single loop of the one-loop maximal secondary canard. The same holds for all of the higher-loop secondary canards, as well. Also, the second loop of the 2-loop canard lies inside the first loop, and it lies extremely close to the second loop of the 3-loop canard. In addition, for even smaller values of the forcing frequency ω, the y-intercepts of the return jumps increase. Moreover, these y-intercepts diverge to ∞ in the limit $\omega \to 0$. In fact, in this limit, the maximal secondary canards collapse onto the primary strong canard, consistent with the observation that the branches of maximal secondary canards emanate from the same FSN I points as the primary canards do.

We now investigate what happens to the invariant slow manifolds near the turning points (recall Fig. 3) of the fold curves of secondary canards. In Fig. 11, we show one such fold curve and take four values of ω, for a fixed value of a, near the turning point which marks the largest ω value of this curve (top panel). For each value of ω,

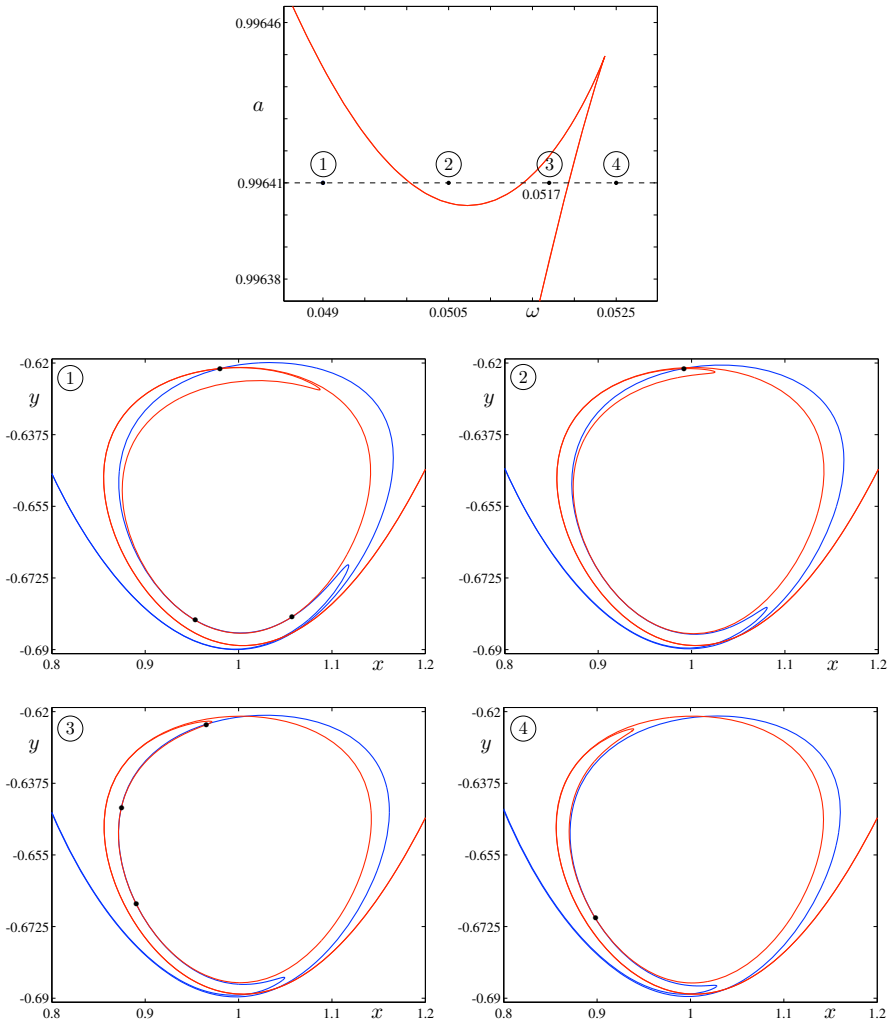

Fig. 11 Evolution of the intersection points (*black dots*) between the curves representing S_a^ε and S_r^ε in a fixed cross section through the folded node. Here, $a = 0.99641$, $b = 0.01$, and $\varepsilon = 0.05$. The values of ω are (*1*) 0.049, (*2*) 0.0505, (*3*) 0.0517, (*4*) 0.0525, as also labelled on the horizontal axis in the top frame. In the transition between frames (*1*) and (*2*), the lower two intersection points disappear. Between frames (*2*) and (*3*), two intersection points are created. Then, two disappear in the final transition shown, from (*3*) to (*4*)

we compute S_a^ε and S_r^ε up to a fixed cross section, following the procedure described above. Then, the intersection curves of both manifolds in the fixed cross section are shown for each ω value in the four bottom panels of Fig. 11. Each time the fold curve of maximal canard solutions is crossed, two intersections of the attracting and repelling slow manifolds disappear or are created. This is illustrated in each of the transitions shown in panels (1)–(4).

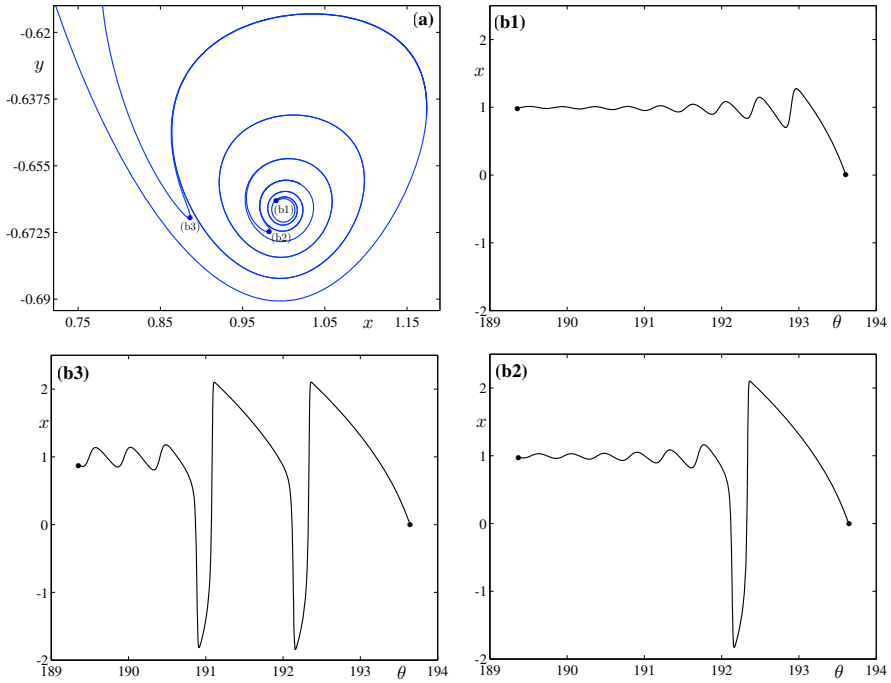

Fig. 12 Repelling slow manifold reversing the direction of spiralling as successive large-amplitude oscillations appear in the orbit. **b1**, **b2**, and **b3** show the solution profiles corresponding to three such events. Here, $a = 0.9935$, $b = 0.01$, $\omega = 0.3$, and $\varepsilon = 0.05$

5.2 Growth of Large-Amplitude Oscillations from Small-Amplitude Oscillations in the Secondary Canards

Along the continuation of the secondary canards, an orbit segment can 'grow' a large-amplitude oscillation. This occurs in regions where the repelling slow manifold spirals backwards instead continuing to spiral inwards towards the weak canard. In Fig. 12, we show the repelling slow manifold for $\overline{\omega} = 0.3$ in the cross section Σ_n; the direction of spiralling changes three times along this portion of the slow manifold, at the points labelled (b1), (b2), and (b3) in frame (a). Each direction reversal corresponds to the orbit growing a large-amplitude oscillation. In panels (b1), (b2), and (b3), we show the profiles of the computed solution segments at these events. Note that the first fold encountered (starting from the centre of the spiral and going outwards) corresponds to the orbit segment having one small-amplitude oscillation grow up to the size of an large-amplitude oscillation (this occurs at the second fold), whilst the other small-amplitude oscillations stop growing in size.

Remark 5 An important consequence of studying the curves of maximal canards and maximal torus canards in the parameter space of (1) is that they serve as the boundaries between different dynamic regimes of (1). As highlighted briefly by the graphical summary in the (ω, a) plane shown in Fig. 4, the fvdP equation (1) exhibits small-

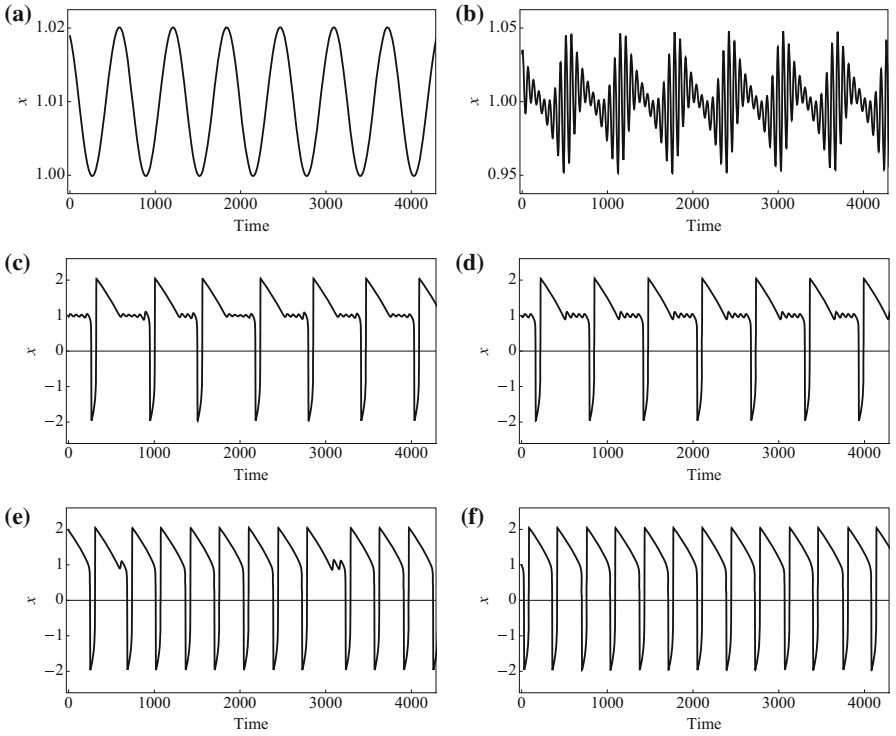

Fig. 13 Transition from small-amplitude oscillations to mixed-mode oscillations to large-amplitude oscillations in the fvdP equation (1). The attractors of (1) are shown for $\varepsilon = 0.01$, $\omega = 0.01$, and **a** $a = 1.01$, **b** $a = 0.9999$, **c** $a = 0.999$, **d** $a = 0.994$, **e** $a = 0.991$, and **f** $a = 0.987$

amplitude oscillations, large-amplitude or relaxation oscillations, and mixed-mode oscillations. The small-amplitude oscillations are the $\frac{2\pi}{\omega}$-periodic solutions generated when an attracting equilibrium of the unforced vdP equation (i.e. $b = 0$) is subjected to a small-amplitude periodic forcing of frequency ω (Fig. 13a). The large-amplitude oscillations occur when the equilibrium of the planar vdP equation sits on the middle branch of the cubic-shaped nullcline and the attractor of the system is a relaxation oscillation that alternates the trajectory between the outer branches of the cubic (Fig. 13f). The mixed-mode oscillations feature small-amplitude oscillations superimposed on large-amplitude relaxation-type oscillations. Figure 4 shows that the mixed-mode oscillations become more robust for low-frequency forcing, just as was observed in numerical simulations of a rotated van der Pol-type model in Benes et al. (2011).

6 The fvdP is a Normal Form for a Class of Systems Near Torus Canard Explosions

In this section, we prove that, under a number of natural conditions, a slow/fast system with two fast variables and one slow variable, which is subject to time-periodic forcing and for which the fast system possesses a generic fold of limit cycles, is equivalent to

a system in which the fast component is given to lowest order by the forced van der Pol system (1). We consider systems with two fast variables and one slow variable of the following form:

$$\begin{aligned} \dot{x} &= f_1(x, y, z) \\ \dot{y} &= f_2(x, y, z) \\ \dot{z} &= \varepsilon\, g(x, y, z), \qquad x, y, z \in \mathbb{R}. \end{aligned} \tag{33}$$

The fast system is

$$\begin{aligned} \dot{x} &= f_1(x, y, z) \\ \dot{y} &= f_2(x, y, z) \end{aligned} \tag{34}$$

in which z is a parameter, and we make the following hypotheses about the fast system:

(H1) For $z = 0$, there exists a non-degenerate periodic solution $\tilde{\Gamma}$; and, here by non-degenerate, we mean a periodic solution with finite period.

(H2) The Floquet multiplier of this periodic orbit at $z = 0$ is one.

Under the hypotheses (H1) and (H2), we prove the following theorem:

Theorem 6.1 *Given (H1), (H2), and a non-degeneracy assumption (see (43) below), system (33) is locally (in a small neighbourhood of $\tilde{\Gamma}$) orbitally equivalent to*

$$\begin{aligned} \dot{\rho} &= z - \rho^2 + O(\rho^3) + O(\varepsilon) \\ \dot{\theta} &= 1 \\ \dot{z} &= \varepsilon\, \tilde{g}(\rho, \theta, z), \qquad \rho, z, \theta \in \mathbb{R}, \end{aligned} \tag{35}$$

where $\tilde{g}$ is 2π-periodic in θ, and z and ρ are small.

The fast subsystem of (35) has very similar dynamics to that of (1); however, the slow system of the general systems may be much richer than the slow system of (1). We make a more detailed comparison between the full systems later in this section. We first analyse the fast systems.

We begin the proof of Theorem 6.1 with some preliminary transformations. On the basis of (H1), one may rectify the flow of (34) so that the periodic orbit becomes the unit circle. Next, using the coordinates

$$x = (1 + r)\cos(\theta) \quad \text{and} \quad y = (1 + r)\sin(\theta),$$

one may transform (34) to

$$\begin{aligned} \dot{r} &= \tilde{f}_1(r, \theta, z) \\ \dot{\theta} &= \tilde{f}_2(r, \theta, z), \end{aligned} \tag{36}$$

where $\tilde{f}_i$ is 2π periodic in θ, $\tilde{f}_1(0, \theta, 0) = 0$, and $\tilde{f}_2 \neq 0$ in a neighbourhood of $(0, \theta, 0)$. Also, one may scale the time variable so that (36) becomes

$$\begin{aligned} \dot{r} &= F(r, \theta, z) \\ \dot{\theta} &= 1, \end{aligned} \tag{37}$$

with $F = \tilde{f}_1 / \tilde{f}_2$. This is a useful formulation of the fast system, and we work directly with this throughout the proof.

In order to analyse the dynamics of this system for small values of r, we expand:

$$F(r, \theta, z) = \psi_0(\theta, z) + r\psi_1(\theta, z) + r^2\psi_2(\theta, z) + \cdots + r^N\psi_N(\theta, z) + O(r^{N+1}). \tag{38}$$

Condition (H2) is now equivalent to

$$\int_0^{2\pi} \psi_1(\theta, 0) \mathrm{d}\theta = 0, \tag{39}$$

because

$$\frac{\partial \bar{F}}{\partial r}(0, 0) = 0,$$

where the average of F is defined as

$$\bar{F}(r, z) = \frac{1}{2\pi} \int_0^{2\pi} F(r, \theta, z) \mathrm{d}\theta.$$

Also, to analyse the dynamics for small values of r, it is useful to introduce a new variable ρ by

$$r = \phi_0 + \rho \mathrm{e}^{\phi_1} + \rho^2\phi_2 + \cdots + \rho^N\phi_N, \quad N \geq 2. \tag{40}$$

where ϕ_i are functions of (θ, z) to be determined.

The following lemma lies at the heart of the proof of this theorem:

Lemma 6.2 *There exists a choice of functions ϕ_i, $i = 1, \ldots, N$, in the coordinate change (40) and a function $G(\rho, z)$ such that, in the coordinates (ρ, θ), the fast system (37) has the form*

$$\begin{aligned} \dot{\rho} &= G(\rho, z) + O(\rho^{N+1}) \\ \dot{\theta} &= 1. \end{aligned} \tag{41}$$

Remark 6 Hypothesis (H2) is not needed for this lemma. Lemma 6.2 says that there exists a near-identity transformation that makes (37) independent of θ up to $\mathcal{O}(\rho^{N+1})$. The particular choice of the coefficient of the linear ρ term e^{ϕ_1} in (40) more readily facilitates computations involving the Floquet multipliers (i.e. hypothesis (H2)).

Proof See "Appendix 2".

Proof of Theorem 6.1 If we apply the sequence of transformations leading to (41) to system (33), we obtain a system of the form

$$\begin{aligned} \dot{\rho} &= G(\rho, z) + O(\rho^{N+1}) + O(\varepsilon) \\ \dot{\theta} &= 1 \\ \dot{z} &= \varepsilon\, \tilde{g}(\rho, \theta, z, \varepsilon). \end{aligned} \tag{42}$$

with

$$G(\rho, z) = \sum_{j=0}^{N-1} \lambda_j(z)\rho^j$$

and the coefficient functions are as introduced in the proof of Lemma 6.2. In particular, hypotheses **(H1)** and **(H2)** imply $\lambda_0(0) = 0$ and $\lambda_1(0) = 0$. We now formulate the additional degeneracy assumptions in terms of the functions λ_j. We will assume that $N \geq 3$.

$$\begin{aligned} \frac{\mathrm{d}\lambda_0}{\mathrm{d}z}(0) &\neq 0. \\ \lambda_2(0) &\neq 0. \end{aligned} \tag{43}$$

If (43) holds in addition to **(H1)** and **(H2)** we replace the variable z by $\tilde{z} = \lambda_0(z)$ and perform scalings and translations to arrive at (35), taking ε sufficiently small as necessary. □

We now make some remarks relating the normal form equation (35) derived in this section and the fvdP equation (1). Clearly, the fast subsystems are similar. If in addition to (43) we assume that $\lambda_3(0) \neq 0$ and make some assumptions about the signs of the coefficients, then the two fast systems are the same to lowest order (up to a simple transformation). The situation with the slow equation is more complicated. In systems with time-periodic forcing, we have shown that (1) is a normal form. Moreover, because forced systems are not generic in the larger class of general slow/fast dynamical systems, we expect the dynamics in this larger class to be even richer. In addition, if we assume that $\tilde{g}(0, \theta_0, 0, 0) = 0$ for some $\theta_0 \in [0,\ 2\pi)$, then we may obtain some canard dynamics. In general, these slow/fast systems will have folded singularities and associated canard dynamics.

7 Conclusions and Discussion

In this article, we have established the existence of a number of different types of canard solutions of the fvdP equation (1) across the entire range of forcing frequencies $\omega > 0$. Most interestingly, we have found numerically that the families of primary maximal canards and maximal torus canards are organised along single branches in parameter space. In the low-frequency regime ($\omega = \mathcal{O}(\varepsilon)$), Theorem 1.1 demonstrates the existence of the primary maximal canards of the FSN I points and establishes that formula (2) gives the loci of the folds of the primary maximal canards in the $(a, b, \overline{\omega})$

parameter space with $b = \mathcal{O}(\sqrt{\varepsilon})$. In the intermediate-frequency regime ($\omega = \mathcal{O}(\sqrt{\varepsilon})$) and high-frequency regime ($\omega = \mathcal{O}(1)$), Theorem 1.2 and Corollary 1.3, respectively, establish the existence of maximal torus canards as well as the formulas (3) and (4), which explicitly give the locations of the folds of the maximal torus canards in the (a, b, ω) parameter space with $b = \mathcal{O}(\varepsilon)$. These maximal torus canards lie precisely in the intersection of the persistent critical manifolds of attracting limit cycles and of repelling limit cycles. They are the analogs in one higher dimension of the maximal canard cycles of the unforced van der Pol equation, see for example Benoit et al. (1981), Dumortier and Roussarie (1996), Eckhaus (1983). Moreover, they are similar to the folds of maximal torus canards observed earlier in a rotated system of van der Pol type, see Figure 5 in Benes et al. (2011).

It was also shown that these analytical results are all representations of the same formula (6) that holds across the entire range of forcing frequencies $\omega > 0$ for the appropriate values of b and that these formulas agree well with the results obtained from numerical continuations over the parameter regions in which they apply. Moreover, in the limit $\omega \to \infty$, the torus canards appear to be rotated copies of the limit cycle canards that exist in the planar unforced van der Pol equation, and the interval of a values for which the maximal torus canards exist shrinks to the value $a_c(\varepsilon) = 1 - \frac{\varepsilon}{8}$ at which the maximal canard solution exists in the unforced equation, recall (Baer and Erneux 1986; Benoit et al. 1981; Braaksma 1993; Dumortier and Roussarie 1996; Eckhaus 1983).

It is worth noting that the analytical results presented here for the torus canards of (1) agree with and expand upon by the general topological analysis presented in Section 6 of Burke et al. (2012). There, fast–slow systems with two fast variables and one slow variable were studied in which there is a torus canard explosion in the transition regime from stable periodic spiking (tonic spiking) to bursting, and examples were given, including of the Hindmarsh–Rose equation, the Morris–Lecar–Terman model, and the Wilson–Cowan–Izhikevich system. In particular, it was shown using topological arguments that there must be a sequence of torus canards in these transition regimes in order to satisfy the property of continuous dependence of solutions on parameters. The topological analysis presented in Burke et al. (2012) is the analog in one higher dimension of the topological analysis first used in Benoit et al. (1981) to establish the existence of an explosion of limit cycle canards in the transition between asymptotically stable solutions and full-blown relaxation oscillations in the unforced, planar van der Pol equation.

In this article, we also studied the branches of the secondary maximal canards, which exist in the low-frequency regime in (1). Secondary canards lie close to the primary strong canard for most of their lengths, and in addition, they make finitely many loops near the bottom of Γ, recall Fig. 7. They are indexed by the number of loops and by the height in the y variable of the jumps from the repelling slow manifold back to the attracting slow manifold. We showed how the dynamics of these secondary canards changes as the parameters change along the fold curves, and we identified the mechanism by which these branches turn around well before they get into the high-frequency regime. In particular, the turning points correspond precisely to the parameter values at which the fold curve of maximal canards is crossed and two intersection points of the attracting and repelling slow manifolds are created (or

annihilated). In addition, we identified how new large-amplitude oscillation segments are added to the secondary canard solutions at points at which the direction of spiralling of the repelling slow manifold is reversed, recall Fig. 9.

Finally, we proved that the fvdP equation (1) is a normal form for a class of slow/fast systems with two fast variables and one slow variable, which possess a non-degenerate fold of limit cycles in the fast system and which exhibit the torus canard explosion phenomenon. Thus, the methods and results obtained here for (1) extend naturally to a large class of slow/fast systems with single-frequency time-periodic forcing.

To conclude this article, we discuss a number of topics related to the canard solutions of the fvdP (1). First, the fold curves of the primary maximal canards in the low-frequency regime and the fold curves of the maximal torus canards in the intermediate- and high-frequency regimes together serve as the boundary of the regime of mixed-mode oscillations in (1), recall Figs. 4 and 13.

Second, there are many different branches of resonance curves, curves of torus bifurcations, saddle nodes of periodic orbits, period-doubling curves of periodic orbits, and so forth, all of which lie in the interior of the region of mixed-mode oscillations in parameter space. These bifurcation curves play important roles as the boundaries between orbit segments with different numbers of small- and large-amplitude oscillations. These are the subject of future work.

Third, in general planar slow/fast systems the formula for classical maximal limit cycle canards is typically obtained as a power series in $\sqrt{\varepsilon}$. The coefficients in this expansion can be obtained using the first Lyapunov coefficient of the Hopf bifurcation. We refer the reader to Kuehn (2010, 2015) for a general treatment. Only in special cases such as planar vdP does this expansion simplify. Similarly, the computation of the maximal torus canards presented herein simplifies due to the simple form of the fvdP equation. Extending the analysis of this work to more general slow/fast systems is the subject of ongoing research.

Acknowledgments The research of J.B., T.J.K., and T.V. was partially supported by NSF-DMS 1109587. T.J.K. thanks INRIA for their hospitality and for providing a climate highly conducive to research and collaboration during a visit. The authors thank Nick Benes, Mark Kramer, Christian Kuehn, John Mitry, and Martin Wechselberger for useful conversations.

Appendix 1: Proof of the Existence of a Torus Bifurcation

In this appendix, we consider the fvdP oscillator (1) subject to high-frequency forcing ($\omega = \mathcal{O}(1)$). In this case, y is the only slow variable, and there is no critical manifold. As such, the fast dynamics are dominant throughout the phase space, and system (1) can be interpreted as a regularly perturbed, non-autonomous problem.

We establish the existence of a torus bifurcation using second-order averaging and equivariant normal form theory in "Second-Order Averaging and a Torus Bifurcation in the Regime $\omega = \mathcal{O}(1)$" section in "Appendix 1", and we present the asymptotics of the torus bifurcation parameter value $a_{\mathrm{TB}}(b, \omega, \varepsilon)$ in "Asymptotic Expansion of $a_{\mathrm{TB}}(b, \omega, \varepsilon)$" section in "Appendix 1".

Second-Order Averaging and a Torus Bifurcation in the Regime $\omega = \mathcal{O}(1)$

In this section, we perform a standard second-order averaging analysis of system (1) and use equivariant normal form theory in the regime $\omega = \mathcal{O}(1)$ to demonstrate that there exists a smooth function $a = a_{\mathrm{TB}}(b, \omega, \varepsilon)$ at which the system possesses a torus bifurcation in which a stable two-torus is born. First, we change variables so that the fold is located at the origin: $(\tilde{x}, \tilde{y}) = (1 - x, y + \frac{2}{3})$ and $\alpha = a - 1$. The fvdP equation transforms to

$$\begin{aligned} \tilde{x}' &= -\tilde{y} + \tilde{x}^2 - \frac{1}{3}\tilde{x}^3 \\ \tilde{y}' &= \varepsilon\,(\tilde{x} + \alpha + b\cos\theta) \\ \theta' &= \omega. \end{aligned}$$

Then, to carry out the second-order averaging analysis, it is natural to use the following scaling, which comes from the central chart of the desingularisation, or blow-up, analysis used in Sect. 4 and in Krupa and Szmolyan (2001):

$$\tilde{x} = \sqrt{\varepsilon}\,\bar{x}, \quad \tilde{y} = \varepsilon\,\bar{y}, \quad b = \sqrt{\varepsilon}\,\bar{b}, \quad \alpha = \sqrt{\varepsilon}\,\bar{\alpha},$$

and to rescale time by $t \longrightarrow \omega t$. Hence, after dropping the bars, the system has the following non-autonomous form:

$$\begin{aligned} \dot{x} &= \frac{\delta}{\omega}\left(-y + x^2\right) - \frac{\delta^2}{3\omega}x^3 \\ \dot{y} &= \frac{\delta}{\omega}\left(x + \alpha + b\cos(t_0 + t)\right), \end{aligned} \tag{44}$$

where $\delta = \sqrt{\varepsilon}$. The choice of t_0 has no effect on the analysis.

Next, we apply the near-identity change in variables used in second-order averaging (Guckenheimer and Holmes 1983; Sanders and Verhulst 1985), so that system (44) transforms into

$$\begin{aligned} \dot{\xi}_1 &= \frac{\delta}{\omega}\left(-\xi_2 + \xi_1^2\right) - \frac{\delta^2}{3\omega}\xi_1^3 + \tilde{G}(\xi_1, \xi_2, t, \delta) \\ \dot{\xi}_2 &= \frac{\delta}{\omega}\left(\xi_1 + \alpha\right) + O(\delta^3), \end{aligned} \tag{45}$$

with $\tilde{G}(\xi_1, \xi_2, t, \delta) = O(\delta^3)$. We label (45) as the 'intermediate' system; it is smoothly conjugate to the original system.

We are interested in the averaged system,

$$\begin{aligned} \dot{\bar{x}} &= \frac{\delta}{\omega}\left(-\bar{y} + \bar{x}^2\right) - \frac{\delta^2}{3\omega}\bar{x}^3 \\ \dot{\bar{y}} &= \frac{\delta}{\omega}\left(\bar{x} + \alpha\right). \end{aligned} \tag{46}$$

This system has a unique $\mathbb{S}^1$ equivariant normal form (Golubitsky et al. 1988) due to its symmetry properties. Moreover, the time-T map of this normal form must be the

$\mathbb{S}^1$ normal form of the time-T map, since the two operations commute and since $\mathbb{S}^1$ equivariant normal forms are unique. Let $\bar{\mathfrak{s}}$ denote the Poincare map of this normal form. At $\alpha = 0$, the eigenvalues of the map $\bar{\mathfrak{s}}$ satisfy the non-resonance condition: they are not equal to the first four strong resonant eigenvalues. Also, the second Lyapunov coefficient is negative; in fact, for the averaged system, the second Lyapunov coefficient is known to be $K\delta$, where $K < 0$ is a constant. Hence, at $\alpha = 0$, the map $\bar{\mathfrak{s}}$ satisfies the basic hypotheses of the Hopf bifurcation for maps; see conditions A and B, respectively, and Theorem 2 of Lanford (1973). Therefore, at $\alpha = 0$, the map $\bar{\mathfrak{s}}$ undergoes a non-degenerate, supercritical Hopf bifurcation in which a normally hyperbolic invariant circle is created. Hence, one also sees directly that the averaged system (46) undergoes a torus bifurcation at $\alpha = 0$ in which the limit cycle becomes unstable and a stable invariant torus is created.

We now demonstrate that the full system (44) undergoes a torus bifurcation at some α_{TB} near $\alpha = 0$, in which a stable invariant torus is created. In particular, we show that the Poincare map $\mathfrak{s}$ of the full system (44) possesses an invariant circle δ-close to the one of $\bar{\mathfrak{s}}$.

First, we observe that the same near-identity coordinate change employed above to put the averaged system (46) into its $\mathbb{S}^1$ equivariant normal form also puts the intermediate system (45) into its $\mathbb{S}^1$ equivariant normal form, up to and including $\mathcal{O}(\delta^2)$. Let $\mathfrak{s}_i(z)$ denote the Poincare map of this normal form. Again, this map must be the time-T map of the normal form, due to uniqueness in the $\mathbb{S}^1$ equivariant case. Next, we observe that, by standard second-order averaging theory, the Poincare maps are close, i.e. on time intervals of length $\mathcal{O}(1/\delta)$,

$$|\mathfrak{s}_i(z) - \bar{\mathfrak{s}}(z)| = \mathcal{O}(\delta).$$

In fact, for each α sufficiently small, the map $\mathfrak{s}_i$ is part of exactly the type of one-parameter family of maps studied in Lanford (1973), with the map of the averaged system being the 'unperturbed' map. Hence, for some α near $\alpha = 0$, the map $\mathfrak{s}_i$ also undergoes a non-degenerate, super-critical Hopf bifurcation in which a normally-attracting invariant circle is created.

Finally, we observe that the time-T maps $\mathfrak{s}$ and $\mathfrak{s}_i$ are smoothly conjugate. Hence, it follows that the map $\mathfrak{s}$ of the original system (44) also has a non-degenerate Hopf bifurcation and therefore that the original vector field (44) has a torus bifurcation at some α_{TB} near zero, in which an attracting invariant torus is created. This concludes the demonstration.

Remark 7 One boundary of the parameter α for the existence of an invariant torus for the full system is given by the birth of the canard regime.

Asymptotic Expansion of $a_{\mathrm{TB}}(b, \omega, \varepsilon)$

In this section, we present the asymptotic expansion of $a = a_{\mathrm{TB}}(b, \omega, \varepsilon)$ for small b. The unforced vdP equation has an equilibrium at $(x, y) = (a, f(a))$, which undergoes a Hopf bifurcation at $a = 1$. This corresponds to a periodic orbit of (1) at $b = 0$ which

undergoes a torus bifurcation at $a = 1$. We seek periodic solutions of (1) as an asymptotic series in b, i.e. let

$$x(t) = \sum_{k=0}^{\infty} b^k x_k(t), \quad y(t) = \sum_{k=0}^{\infty} b^k y_k(t).$$

Substitution into (1) yields

$$\begin{aligned} \dot{x}_0 &= y_0 - f(x_0), \\ \dot{y}_0 &= \varepsilon(a - x_0), \end{aligned}$$

at leading order, which is the planar van der Pol equation. This has an equilibrium at $(x, y) = (a, f(a))$. The $\mathcal{O}(b^1)$ system is

$$\begin{aligned} \dot{x}_1 &= y_1 - f'(x_0)\, x_1, \\ \dot{y}_1 &= \varepsilon(-x_1 + \cos \omega t). \end{aligned}$$

The $\mathcal{O}(b^1)$ system is linear with solutions that are linear combinations of $\cos \omega t$, $\sin \omega t$, and $\exp(\lambda t)$, where $2\lambda = 1 - a^2 \pm \sqrt{(1-a^2)^2 - 4\,\varepsilon}$.

Remark 8 Note that when $a = 1$ and $\omega = \sqrt{\varepsilon}$, there is a resonance.

When a damped oscillator is driven with a periodic forcing function, the result may be a periodic response at the same frequency as the forcing function (see Fig. 13a). Since the unforced oscillation is dissipated due to the damping, it is absent from the steady state behaviour. Thus, we seek periodic solutions of the $\mathcal{O}(b^1)$ system of period $T = \frac{2\pi}{\omega}$. The solutions are

$$\begin{aligned} x_1(t) &= \frac{\left(a^2-1\right)\varepsilon\omega \sin(t\omega) + \varepsilon\left(\varepsilon - \omega^2\right)\cos(t\omega)}{\left(a^2-1\right)^2\omega^2 + \left(\varepsilon-\omega^2\right)^2}, \\ y_1(t) &= \frac{\varepsilon\left(\left(a^2-1\right)\varepsilon\cos(t\omega) + \omega\left(a^4 - 2a^2 - \varepsilon + \omega^2 + 1\right)\sin(t\omega)\right)}{\left(a^2-1\right)^2\omega^2 + \left(\varepsilon-\omega^2\right)^2}. \end{aligned}$$

We now compute the stability of a periodic solution of (1). Let (x_γ, y_γ) denote the periodic solution and let $(u, v) = (x - x_\gamma, y - y_\gamma)$ be a perturbation of this orbit. Then the perturbations evolve according to

$$\begin{pmatrix} \dot{u} \\ \dot{v} \end{pmatrix} = Df(x_\gamma, y_\gamma)\begin{pmatrix} u \\ v \end{pmatrix} - \begin{pmatrix} \frac{1}{2}f''(x_\gamma)u^2 + \frac{1}{6}f'''(x_\gamma)u^3 \\ 0 \end{pmatrix},$$

where the Jacobian evaluated along (x_γ, y_γ) is the T-periodic matrix:

$$Df(x_\gamma, y_\gamma) = \begin{pmatrix} -f'(x_\gamma) & 1 \\ -\varepsilon & 0 \end{pmatrix}.$$

The Floquet multipliers ρ_1 and ρ_2 satisfy

$$\rho_1 \rho_2 = \exp\left(\int_0^{\mathrm{T}} \operatorname{tr} Df(x_\gamma, y_\gamma)\, \mathrm{d}t\right).$$

A Neimark–Sacker bifurcation occurs when the multipliers are $\rho = \mathrm{e}^{\pm i\mu}$ for some μ. That is, a torus bifurcation occurs when $\int_0^{\mathrm{T}} \operatorname{tr} Df(x_\gamma, y_\gamma)\, \mathrm{d}t = 0$. This gives the following relation between a, b, ε, and ω for the location of the torus bifurcation:

$$1 - a^2 - \frac{1}{2}\frac{b^2\,\varepsilon^2}{(a^2-1)^2\omega^2 + (\varepsilon - \omega^2)^2} = 0. \tag{47}$$

Comparisons between the theoretical prediction above and the results of numerical continuation simulations show good agreement for the indicated parameter regions. Divergence from the above perturbation analysis occurs precisely at the resonances (figures not shown).

Remark 9 Note that (47) is accurate up to terms of order $\mathcal{O}(b^3)$. That is, there are no order $\mathcal{O}(b^2)$ corrections in (47) from the $b^2 x_2$ terms in the asymptotic expansion due to symmetry. More precisely, symmetry considerations give

$$-2ab^2 \int_0^{\mathrm{T}} x_2\, \mathrm{d}t = 0.$$

Appendix 2: Proof of Lemma 6.2

The proof is split into three steps. First, we consider the simplest case in which $N = 1$ in (40). Next, we prove the Theorem for $N = 2$, and finally, we prove it for general N in (40). The near-identity coordinate change employed in the following proof is similar to the near-identity coordinate changes typically used in the general theory of averaging (Sanders and Verhulst 1985).

Step 1. With $N = 1$, the relevant transformation (40) between r and ρ is:

$$r = \phi_0 + \rho \mathrm{e}^{\phi_1}. \tag{48}$$

Differentiating (48) with respect to time, substituting in (37), and Taylor expanding $F(\phi_0 + \rho \mathrm{e}^{\phi_1}, \theta, z)$ about ϕ_0, we obtain

$$\dot{\rho} = (-\phi_{0,\theta} + F(\phi_0, \theta, z))\mathrm{e}^{-\phi_1} + \rho(-\phi_{1,\theta} + F_r(\phi_0, \theta, z)) + O(\rho^2). \tag{49}$$

Hence, based on the form of the two sets of terms in parentheses in the right member of this equation, we are naturally led to study the following system of two ordinary differential equations with two unknown parameters:

$$\begin{aligned} \phi_{0,\theta} &= F(\phi_0, \theta, z) + \lambda_0 \mathrm{e}^{\phi_1} \\ \phi_{1,\theta} &= F_r(\phi_0, \theta, z) + \lambda_1 \end{aligned} \tag{50}$$

In this manner, proving the result for $N = 1$ is now equivalent to finding λ_0 and λ_1 for which there exist ϕ_0 and ϕ_1 which are 2π periodic and which satisfy the equation (50).

According to general theory of differential equations, for every pair (λ_0, λ_1), there exists a unique solution (ϕ_0, ϕ_1) of (50) satisfying the initial conditions $\phi_0(0) = 0$ and $\phi_1(0) = 0$. Such solutions must satisfy the integral equations,

$$\begin{aligned} \phi_0(\theta) &= \int_0^\theta F(\phi_0(\nu), \nu, z)\mathrm{d}\nu + \lambda_0 \int_0^\theta \mathrm{e}^{\phi_1(\nu)}\mathrm{d}\nu \\ \phi_1(\theta) &= \int_0^\theta F_r(\phi_0(\nu), \nu, z)\mathrm{d}\nu + \lambda_1\theta. \end{aligned} \tag{51}$$

Also, in terms of these integral equations, the conditions for periodicity of ϕ_0 and ϕ_1 (with respect to θ) are

$$\begin{aligned} 0 &= \int_0^{2\pi} F(\phi_0(\nu), \nu, z)\mathrm{d}\nu + \lambda_0 \int_0^{2\pi} \mathrm{e}^{\phi_1(\nu)}\mathrm{d}\nu \\ 0 &= \int_0^{2\pi} F_r(\phi_0(\nu), \nu, z)\mathrm{d}\nu + 2\pi\lambda_1. \end{aligned} \tag{52}$$

Based on the above formulation of the integral equations, it is useful to define $\mathcal{H}\colon \mathbb{R} \times \mathbb{R}^2 \to \mathbb{R}^2$, as follows:

$$\mathcal{H}(z, \lambda_0, \lambda_1) = \begin{pmatrix} \mathcal{H}_0(z, \lambda_0, \lambda_1) \\ \mathcal{H}_1(z, \lambda_0, \lambda_1) \end{pmatrix} = \begin{pmatrix} \int_0^{2\pi} F(\phi_0(\nu), \nu, z)\mathrm{d}\nu + \lambda_0 \int_0^{2\pi} \mathrm{e}^{\phi_1(\nu)}\mathrm{d}\nu \\ \int_0^{2\pi} F_r(\phi_0(\nu), \nu, z)\mathrm{d}\nu + 2\pi\lambda_1 \end{pmatrix}. \tag{53}$$

Now, by the assumptions (H1) and (H2) (see (39)), $\lambda_0 = 0$, $\lambda_1 = 0$, and $z = 0$ is a solution of (51) with $\phi_0 = 0$ and $\phi_{1,0} = \int_0^\theta F_r(0, \nu, 0)\mathrm{d}\nu$. We now verify that the assumptions of the implicit function theorem are satisfied to show that there is a branch of non-trivial solutions emanating from this trivial solution. In particular, we verify that $D\mathcal{H}(0, 0, 0)$ is non-singular, by showing that $\det D\mathcal{H}(0, 0, 0) = (2\pi)^2$.

From the definition, we see that $\mathcal{H}_{1,\lambda_1}(0, 0, 0) = 2\pi$. We will now show that $\mathcal{H}_{0,\lambda_1}(0, 0, 0) = 0$ and $\mathcal{H}_{0,\lambda_0}(0, 0, 0) = 2\pi$. To show that $\mathcal{H}_{0,\lambda_1}(0, 0, 0) = 0$, we start with

$$\mathcal{H}_{0,\lambda_1}(0, 0, 0) = \int_0^{2\pi} F_r(0, \theta, 0)\phi_{0,\lambda_1}(\theta)\mathrm{d}\theta.$$

Then, using (50), we obtain

$$\mathcal{H}_{0,\lambda_1}(0, 0, 0) = \int_0^{2\pi} \frac{\mathrm{d}}{\mathrm{d}\theta}\phi_{0,\lambda_1}(\theta)\mathrm{d}\theta = \phi_{0,\lambda_1}(2\pi) - \phi_{0,\lambda_1}(0).$$

By assumption (above formula (51)), $\phi_0(0) = 0$ and $\phi_1(0) = 0$ for λ_0 and λ_1. Hence, $\phi_{0,\lambda_j}(0) = 0$ for $j = 1, 2$. Therefore, we conclude from (50) that $\phi_{0,\lambda_1} \equiv 0$, so that this entry of the Jacobian of $\mathcal{H}$ vanishes, as claimed.

Next, we show that $\mathcal{H}_{0,\lambda_0}(0, 0, 0) = 2\pi$. By an argument similar to the above,

$$\mathcal{H}_{0,\lambda_0}(0, 0, 0) = \phi_{0,\lambda_0}(2\pi) - \phi_{0,\lambda_0}(0) = \phi_{0,\lambda_0}(2\pi).$$

Therefore, from (50), we obtain

$$\frac{\mathrm{d}}{\mathrm{d}\theta}\left(\phi_{0,\lambda_0}\right) = F_r(0, \theta, 0)\phi_{0,\lambda_0} + \mathrm{e}^{\phi_1}. \tag{54}$$

Observe that, for $\lambda_0 = 0$ and $\lambda_1 = 0$, we have $\mathrm{d}\phi_1/\mathrm{d}\theta = F_r(0, \theta, 0)$. Hence, (54) is equivalent to

$$\frac{\mathrm{d}}{\mathrm{d}\theta}\left(\phi_{0,\lambda_0}\right) = \frac{d\phi_1}{\mathrm{d}\theta}\phi_{0,\lambda_0} + \mathrm{e}^{\phi_1}, \tag{55}$$

from which it follows that

$$\frac{\mathrm{d}}{\mathrm{d}\theta}\left(\phi_{0,\lambda_0}\mathrm{e}^{-\phi_1}\right) = 1.$$

Finally, since $\phi_{0,\lambda_0}(0) = 0$, it follows from (39) that $\phi_{0,\lambda_0}(2\pi) = 2\pi$. Therefore,

$$\det(D\mathcal{H}(0, 0)) = (2\pi)^2,$$

and by the implicit function theorem, there is a branch of periodic solutions ϕ_0 and ϕ_1 for each (λ_0, λ_1) sufficiently small, emanating from the trivial solution. Therefore, by (49) and (50), one has the equation

$$\dot{\rho} = -\lambda_0 - \lambda_1\rho + \mathcal{O}(\rho^2),$$

which establishes (41) in the case $N = 1$. This completes the proof of the Lemma for the case $N = 1$.

Step 2. We now show that the lemma holds for $N = 2$ in (40). All quantities are expanded up to and including ρ^2. For the vector field F, we have

$$\begin{aligned} F(r, \theta, z) = {} & F(\phi_0, \theta, z) + \rho F_r(\phi_0, \theta, z)\mathrm{e}^{\phi_1} + \rho^2(F_r(\phi_0, \theta, z)\phi_2 \\ & + \frac{1}{2}F_{rr}(\phi_0, \theta, z)\mathrm{e}^{2\phi_1}) + \mathcal{O}(\rho^3). \end{aligned} \tag{56}$$

Also, differentiating (40) for $N = 2$ with respect to t, we find

$$\dot{r} = \dot{\rho}(\mathrm{e}^{\phi_1} + 2\rho\phi_2) + \phi_{0,\theta} + \rho\mathrm{e}^{\phi_1}\phi_{1,\theta} + \rho^2\phi_{2,\theta}. \tag{57}$$

Hence, combining (56) and (57), we get

$$\dot{\rho}(1+2\rho\phi_2 e^{-\phi_1}) = (-\phi_{0,\theta} + F(\phi_0,\theta,z))e^{-\phi_1} + \rho(-\phi_{1,\theta} + F_r(\phi_0,\theta,z)) + \rho^2(-\phi_{2,\theta} + F_r(\phi_0,\theta,z)\phi_2 + \frac{1}{2}F_{rr}(\phi_0,\theta,z)e^{2\phi_1})e^{-\phi_1} + \mathcal{O}(\rho^3). \tag{58}$$

Now, after multiplying both sides of (58) by $(1+2\rho\phi_2 e^{-\phi_1})^{-1}$, we examine the structure of the terms at each order of ρ^0, ρ^1, and ρ^2. This suggests that we analyse the following system of differential equations:

$$\begin{aligned} \phi_{0,\theta} &= F(\phi_0,\theta,z) + \lambda_0 e^{\phi_1} \\ \phi_{1,\theta} &= F_r(\phi_0,\theta,z) - 2\lambda_0\phi_2 e^{-\phi_1} + \lambda_1 \\ \phi_{2,\theta} &= F_r(\phi_0,\theta,z)\phi_2 + \frac{1}{2}F_{rr}(\phi_0,\theta,z)e^{2\phi_1} - 2\lambda_1\phi_2 + \lambda_2 e^{\phi_1}. \end{aligned} \tag{59}$$

The first equation here is equivalent to the first equation in (50); the second has an additional term due to ϕ_2; and the third is new. If we can find a branch of non-trivial solutions of this system, then we can transform the general fast system into the desired form up to and including $\mathcal{O}(\rho^2)$.

As above, we look for 2π periodic solutions. However, before extending the definition of $\mathcal{H}$, we rewrite the third component of (59) as follows:

$$\frac{\mathrm{d}}{\mathrm{d}\theta}\left(\phi_2 e^{-\phi_1}\right) = \frac{1}{2}F_{rr}(\phi_0,\theta,z)e^{\phi_1} + 2\lambda_0\phi_2^2 e^{-2\phi_1} - 3\lambda_1\phi_2 e^{-\phi_1} + \lambda_2. \tag{60}$$

Now, we define $\mathcal{H}\colon \mathbb{R}\times\mathbb{R}^3 \to \mathbb{R}^3$ in a manner similar to that employed in Step 1:

$$\begin{aligned} \mathcal{H}(z,\lambda_0,\lambda_1,\lambda_2) &= \begin{pmatrix} \mathcal{H}_0(z,\lambda_0,\lambda_1,\lambda_2) \\ \mathcal{H}_1(z,\lambda_0,\lambda_1,\lambda_2) \\ \mathcal{H}_2(z,\lambda_0,\lambda_1,\lambda_2) \end{pmatrix} \\ &= \begin{pmatrix} \int_0^{2\pi} F(\phi_0(\nu),\nu,z)\mathrm{d}\nu + \lambda_0\int_0^{2\pi} e^{\phi_1(\nu)}\mathrm{d}\nu \\ \int_0^{2\pi}(F_r(\phi_0(\nu),\nu,z) - 2\lambda_0\phi_2(\nu)e^{-\phi_1(\nu)})\mathrm{d}\nu + 2\pi\lambda_1 \\ \int_0^{2\pi}(\frac{1}{2}F_{rr}(\phi_0(\nu),\nu,z)e^{\phi_1(\nu)} + 2\lambda_0\phi_2(\nu)^2 e^{-2\phi_1(\nu)} - 3\lambda_1\phi_2(\nu)e^{-\phi_1(\nu)} + \lambda_2)\mathrm{d}\nu \end{pmatrix}. \end{aligned} \tag{61}$$

We analyse $\mathcal{H}$ in much the same manner as in Step 1. Observe that, at $z=0$, we have $\lambda_0 = 0$ and $\lambda_1 = 0$. However, λ_2 is in general given by

$$\lambda_2 = -\frac{1}{2\pi}\int_0^{2\pi}\frac{1}{2}F_{rr}(0,\nu,0)e^{\phi_1(\nu)}\mathrm{d}\nu,$$

and not zero.

We now show that the off-diagonal elements of the Jacobian of $\mathcal{H}$ vanish. First, an argument similar to that used in Step 1 shows that $\mathcal{H}_{0,\lambda_1}(0,0,0,\lambda_{2,0}) = 0$. We also need to show that $\mathcal{H}_{0,\lambda_2}(0,0,0,\lambda_{2,0}) = 0$ and $\mathcal{H}_{1,\lambda_2}(0,0,0,\lambda_{2,0}) = 0$. To this end, we prove that $\phi_{0,\lambda_2}(0,0,0,\lambda_{2,0}) \equiv 0$ and $\phi_{1,\lambda_2}(0,0,0,\lambda_{2,0}) \equiv 0$, because then the identities $\mathcal{H}_{0,\lambda_2}(0,0,0,\lambda_{2,0}) = 0$ and $\mathcal{H}_{1,\lambda_2}(0,0,0,\lambda_{2,0}) = 0$ follow in

a straightforward way. We carry out the proof for ϕ_{0,λ_2}; the argument for ϕ_{1,λ_2} is similar. Differentiating the first equation in (59) with respect to λ_2 and using the fact that $\lambda_0\,|_{z=0} = 0$, we obtain

$$\left.\frac{d\phi_{0,\lambda_2}}{\mathrm{d}\theta}\right|_{z=0} = F_r(0,\theta,0)\phi_{0,\lambda_2}|_{z=0}. \tag{62}$$

The claim now follows from the assumption $\phi_0(0, z, \lambda_0, \lambda_1, \lambda_2) \equiv 0$.

Based on the above analysis, it follows that

$$\det(D\mathcal{H}(0,0,0,0)) = \mathcal{H}_{0,\lambda_0}(0,0,0,0)\mathcal{H}_{1,\lambda_1}(0,0,0,0)\mathcal{H}_{2,\lambda_2}(0,0,0,0),$$

and an argument similar to the one used in Step 1 shows that this determinant is nonzero. In particular, $\mathcal{H}_{0,\lambda_0}(0,0,0,0)$ and $\mathcal{H}_{1,\lambda_1}(0,0,0,0)$ are both 2π by a similar calculation. To show that also $\mathcal{H}_{2,\lambda_2}(0,0,0,0) = 2\pi$, we differentiate the third component in (61) to obtain

$$\mathcal{H}_{2,\lambda_2}(0,0,0,0) = \int_0^{2\pi} \mathrm{d}\nu = 2\pi.$$

Hence, we may again use the implicit function theorem to conclude that there exists a branch of non-trivial solutions of (59), and the system may be put in the desired form of (41) up to and including terms of ρ^2. This completes the proof of Lemma 6.2 for the case $N = 2$.

Step 3. In this third and final step of the proof, we show that the lemma holds for general N in (40). We begin by writing

$$F(r,\theta,z) = \sum_{j=0}^{N} \rho^j F_j(\phi_0,\phi_1,\ldots,\phi_N,\theta,z) + O(\rho^{N+1}), \tag{63}$$

where $N > 2$ is a natural number and r and ρ are related by formula (40) associated with this choice of N. For each j, the functions F_j are complicated expressions involving $\phi_0, \phi_1, \ldots, \phi_j$. To simplify the notation, we write $\Phi_j = (\phi_0, \phi_1, \ldots, \phi_j)$. We will give a more precise description of the functions F_j below. The equivalent of (58) is now

$$\begin{aligned}\dot\rho\left(1 + \sum_{l=2}^{N} l\rho^{l-1}\phi_l \mathrm{e}^{-\phi_1}\right) =& (-\phi_{0,\theta} + F(\phi_0,\theta,z))\mathrm{e}^{-\phi_1} + \rho(-\phi_{1,\theta} + F_r(\phi_0,\theta,z)) \\ &+ \sum_{j=2}^{N} \rho^j(-\phi_{j,\theta} + F_j(\Phi_j,\theta,z))\mathrm{e}^{-\phi_1} + \mathcal{O}(\rho^{N+1}).\end{aligned} \tag{64}$$

Let $\alpha_0 = 1$ and for each $j \geq 1$ set

$$\alpha_j(\phi_0, \ldots, \phi_n) = \frac{1}{j!}\partial_\rho^j \left(\frac{1}{1 + \sum_{l=2}^{n} l\rho^{l-1}\phi_l \mathrm{e}^{-\phi_1}} \right) \Big|_{\rho=0}.$$

Note that, for given j, α_j depends on $\phi_0, \phi_1, \ldots, \phi_{j+1}$. We also write

$$\begin{aligned} E_0 &= (-\phi_{0,\theta} + F(\phi_0, \theta, z))\mathrm{e}^{-\phi_1} \\ E_1 &= -\phi_{1,\theta} + F_r(\phi_0, \theta, z) \\ E_2 &= (-\phi_{2,\theta} + F_2(\Phi_2, \theta, z))\mathrm{e}^{-\phi_1} \\ &\vdots \\ E_N &= (-\phi_{N,\theta} + F_N(\Phi_N, \theta, z))\mathrm{e}^{-\phi_1}. \end{aligned} \tag{65}$$

It follows that (64) may be written in the following compact and insightful manner:

$$\dot{\rho} = \sum_{l=0}^{N} \rho^l \left(\sum_{j=0}^{l} \alpha_j E_{l-j} \right) + \mathcal{O}(\rho^{N+1}). \tag{66}$$

We now define the set of equations

$$\begin{aligned} E_0 &= \lambda_0 \\ E_1 + \alpha_1 E_0 &= \lambda_1 \\ E_2 + \alpha_1 E_1 + \alpha_2 E_0 &= \lambda_2 \\ &\vdots \\ \sum_{j=0}^{N} \alpha_j E_{N-j} &= \lambda_N. \end{aligned} \tag{67}$$

This enables us to rewrite (65) as follows:

$$\begin{aligned} E_0 &= \lambda_0 \\ E_1 &= \lambda_1 - \alpha_1\lambda_0 \\ E_2 &= \lambda_2 - \alpha_1\lambda_1 + (\alpha_1^2 - \alpha_2)\lambda_0 \\ &\vdots \\ E_N &= \sum_{j=0}^{N} \beta_j \lambda_{N-j}, \end{aligned} \tag{68}$$

where $\beta_0 = 1$ and $\beta_1, \ldots, \beta_N$ are coefficients depending on $\alpha_0, \ldots, \alpha_N$. Moreover, β_j depends on $\alpha_0, \ldots, \alpha_j$ only. Therefore, we have arrived at the following system of differential equations:

$$\begin{aligned}
\phi_{0,\theta} &= F(\phi_0, \theta, z) + \lambda_0 e^{\phi_1} \\
\phi_{1,\theta} &= F_r(\phi_0, \theta, z) + \lambda_1 - \alpha_1 \lambda_0 \\
\phi_{2,\theta} &= F_2(\Phi_2, \theta, z) + (\lambda_2 - \alpha_1 \lambda_1 + (\alpha_1^2 - \alpha_2)\lambda_0) e^{\phi_1} \\
&\vdots \\
\phi_{N,\theta} &= F_N(\Phi_N, \theta, z) + \left(\sum_{j=0}^{N} \beta_j \lambda_{N-j} \right) e^{\phi_1},
\end{aligned} \tag{69}$$

which is the analog for general N of the systems of differential equation (50) for $N = 1$ and (59) for $N = 2$.

Before defining $\mathcal{H}$, we rewrite (69) in a manner similar to that which was used above to rewrite (59) (recall also (60)). Noting that

$$F_j(\Phi_j, \theta, z) = F_r(\phi_0, \theta, z)\phi_j + \mathcal{R}(\Phi_{j-1}),$$

we replace the jth equation in (69) by

$$\frac{\mathrm{d}}{\mathrm{d}\theta}\left(\phi_j e^{-\phi_1}\right) = \mathcal{R}(\Phi_{j-1}) e^{-\phi_1} - (\lambda_1 - \alpha_1 \lambda_0)\phi_j e^{-\phi_1} + \left(\sum_{l=0}^{j} \beta_l \lambda_{j-l} \right). \tag{70}$$

We will now define the function $\mathcal{H}$ in a manner analogous to (53) and (61) used in Steps 1 and 2, respectively, for the cases $N = 1$ and $N = 2$. We let

$$(\phi_0(\theta, z, \lambda_1, \ldots, \lambda_N), \phi_1(\theta, z, \lambda_1, \ldots, \lambda_N), \ldots, \phi_N(\theta, z, \lambda_1, \ldots, \lambda_N))$$

be the solutions of (69) depending on the parameters z and $\lambda_0, \ldots, \lambda_N$ that satisfy the initial conditions $\phi_j(0, z, \lambda_1, \ldots, \lambda_N) = 0$, $j = 0, 1, \ldots, N$. Further, we let $\mathcal{H}_0$, $\mathcal{H}_1$, and $\mathcal{H}_2$ be defined as in Step 2, and let

$$\begin{aligned}
&\mathcal{H}_j(z, \lambda_0, \lambda_1, \ldots, \lambda_N) \\
&= \int_0^{2\pi} \left(\mathcal{R}(\Phi_{j-1}) e^{-\phi_1} - (\lambda_1 - \alpha_1 \lambda_0)\phi_j e^{-\phi_1} + \sum_{l=0}^{j} \beta_l \lambda_{j-l} \right) \mathrm{d}\nu, \quad j = 2, 3, \ldots N.
\end{aligned} \tag{71}$$

We first argue that we can solve the set of equations $\mathcal{H}_j(0, \lambda_0, \ldots, \lambda_N)$, $j = 0, 1, \ldots, N$, for a unique N-tuple $(\lambda_{0,0}, \lambda_{1,0}, \ldots, \lambda_{N,0})$. Note that $\lambda_{0,0} = 0$ and $\lambda_{1,0} = 0$, by the same analysis used in Step 2. Hence,

$$\sum_{k=0}^{j} \beta_k \lambda_{j-k}|_{z=0} = \sum_{k=0}^{j-2} \beta_k \lambda_{j-k}|_{z=0}.$$

We argue by induction. Suppose that $\lambda_{0,0}, \ldots, \lambda_{j-1,0}$ and the corresponding $\phi_0, \ldots, \phi_{j-1}$ are determined. Note that $\lambda_{j,0}$ must satisfy

$$\lambda_{j,0} = -\int_0^{2\pi} \left(\mathcal{R}(\Phi_{j-1}) \mathrm{e}^{-\phi_1} + \sum_{l=1}^{j-2} \beta_l \lambda_{j-l,0} \right) \mathrm{d}\nu. \tag{72}$$

Since the right member of (72) depends only on $\lambda_0, \ldots, \lambda_{j-1}$ and $\phi_0, \ldots, \phi_{j-1}$, the value of $\lambda_{j,0}$ is uniquely determined. Similarly, knowing $\lambda_{j,0}$, we can solve (70) for ϕ_j using (70) due to the fact that $\lambda_0 = \lambda_1 = 0$, so that right member of (70) depends only on $\lambda_0, \ldots, \lambda_{j-1}$ and $\phi_0, \ldots, \phi_{j-1}$. Hence, ϕ_j is uniquely determined.

We now prove that $D_{\lambda_0,\ldots,\lambda_N} \mathcal{H}(0, \lambda_{0,0}, \ldots, \lambda_{N,0})$ is non-singular. First, we prove that $\phi_{j,\lambda_k}|_{z=0} = 0$ for any $j \in \{0, \ldots, N-1\}$ and $k \in \{j+1, \ldots, N\}$. The argument for $j = 0$ and $j = 1$ is analogous as in the case of $n = 2$. For general j, we proceed by induction, assuming that the claim holds for $0, 1, \ldots, j-1$. The argument is, again, similar to that used in the case $N = 2$. We differentiate (70) with respect to λ_k and use the induction assumption, the fact that β_j is independent of ϕ_l for any $l > j+1$, and the fact that $\lambda_{0,0} = \lambda_{1,0} = 0$. This gives

$$\frac{\mathrm{d}}{\mathrm{d}\theta} \phi_{j,\lambda_k}(0, \lambda_{0,0}, \ldots, \lambda_{N,0}) = 0. \tag{73}$$

By assumption, $\phi_j(0, z, \lambda_0, \ldots, \lambda_N) \equiv 0$. Hence, the claim follows. Now, differentiating (71) and using a similar procedure, we obtain $\mathcal{H}_{j,\lambda_k}(0, \lambda_{0,0}, \ldots, \lambda_{N,0}) = 0$ for $j \in \{0, \ldots, N-1\}$ and $k \in \{j+1, \ldots, N\}$.

It remains to prove that $\mathcal{H}_{j,\lambda_j}(0, \lambda_{0,0}, \ldots, \lambda_{N,0}) \neq 0$ for $j \in \{0, \ldots, N\}$. The proof for $j = 0$ and 1 is as above. Let $j > 1$. Again by differentiating (71), now with respect to λ_j, and arguing analogously as above, we obtain

$$\mathcal{H}_{j,\lambda_j}(0, \lambda_{0,0}, \ldots, \lambda_{N,0}) = \int_0^{2\pi} \mathrm{d}\nu = 2\pi. \tag{74}$$

We can now apply the implicit function theorem to obtain the functions $\lambda_0(z), \ldots, \lambda_j(z)$ as required. This completes the third (and final) step of the proof of the lemma. □

References

Baer, S., Erneux, T.: Singular Hopf bifurcation to relaxation oscillations. SIAM J. Appl. Dyn. Syst. **46**, 721–739 (1986)

Benes, G.N., Barry, A.M., Kaper, T.J., Kramer, M.A., Burke, J.: An elementary model of torus canards. Chaos **21**, 023131 (2011)

Benoît, E.: Canards et enlacements. Inst. Haut. Etud. Sci. Publ. Math. **72**, 63–91 (1990)

Benoit, E., Callot, J.-L., Diener, F., Diener, M.: Chasse au canard. Collectanea Mathematicae **31–32**, 37–119 (1981)

Bold, K., Edwards, C., Guckenheimer, J., Guharay, S., Hoffman, K., Hubbard, J., Oliva, R., Weckesser, W.: The forced van der Pol equation II: canards in the reduced system. SIAM J. Appl. Dyn. Syst. **2**, 570–608 (2003)

Braaksma, B.: Critical Phenomena in Dynamical Systems of van der Pol type, Ph.D. thesis, University of Utrecht (1993)
Brøns, M., Krupa, M., Wechselberger, M.: Mixed mode oscillations due to the generalized canard phenomenon. In: "Bifurcation Theory and Spatio-Temporal Pattern Formation", Fields Institute Communications, vol. 49, pp. 39–63. American Mathematical Society, Providence, RI (2006)
Burke, J., Desroches, M., Barry, A.M., Kaper, T.J., Kramer, M.A.: A showcase of torus canards in neuronal bursters. J. Math. Neurosci. **2**, 3 (2012)
Cartwright, M.L.: Forced Oscillations in Nonlinear Systems Contrib. to Theory of Nonlinear Oscillations (Study 20), pp. 149–241. Princeton University Press, Princeton (1950)
Cartwright, M.L., Littlewood, J.E.: On non-linear differential equations of the second order: I. The equation $\ddot{y} - k(1 - y^2)\dot{y} + y = b\lambda k \cos(\lambda t + a)$; k large. J. Lond. Math. Soc. **20**, 180–189 (1945)
Delshams, A., Seara, T.M.: An asymptotic expression for the splitting of separatrices of the rapidly forced pendulum. Comm. Math. Phys. **150**(3), 443–463 (1992)
Delshams, A., Seara, T.M.: Splitting of separatrices in Hamiltonian systems with one and a half degrees of freedom. Math. Phys. Electron. J. **3**, 4 (1997)
Desroches, M., Krauskopf, B., Osinga, H.M.: The geometry of slow manifolds near a folded node. SIAM J. Appl. Dyn. Syst. **7**, 1131–1162 (2008)
Desroches, M., Krauskopf, B., Osinga, H.M.: Numerical continuation of canard orbits in slow-fast dynamical systems. Nonlinearity **23**, 739–765 (2010)
Desroches, M., Guckenheimer, J., Kuehn, C., Krauskopf, B., Osinga, H.M., Wechselberger, M.: Mixed-mode oscillations with multiple time scales. SIAM Rev. **54**, 211–288 (2012)
Desroches, M., Krupa, M., Rodrigues, S.: Inflection, canards and excitability threshold in neuronal models. J. Math. Biol. **67**, 989–1017 (2013)
Diener, M.: The canard unchained or how fast–slow systems bifurcate. Math. Intell. **6**, 38–49 (1984)
Doedel, E.J., Champneys, A.R., Fairgrieve, T.F., Kuznetsov, Y.A., Oldeman, K.E., Paffenroth, R.C., Sanstede, B., Wang, X.J., Zhang, C.: AUTO-07P: Continuation and Bifurcation Software for Ordinary Differential Equations. http://cmvl.cs.concordia.ca/ (2007)
Dumortier, F., Roussarie, R.: Canard cycles and center manifolds. Mem. Am. Math. Soc. **577** (1996)
Dumortier, F., Roussarie, R.: Geometric singular perturbation theory beyond normal hyperbolicity. In: Jones, C.K.R.T., Khibnik, A.I. (ed.) Multiple Time Scales Dynamical Systems, IMA Volumes in Mathematics and its Applications, vol. 122, pp. 29–64 (2001)
Eckhaus, W.: Relaxation oscillations including a standard chase on French ducks. Lect. Notes Math. **985**, 449–494 (1983)
Erchova, I., McGonigle, D.J.: Rhythms of the brain: an examination of mixed mode oscillation approaches to the analysis of neurophysiological data. Chaos **18**, 015115 (2008)
Fenichel, N.: Geometric singular perturbation theory for ordinary differential equations. J. Differ. Eqs. **31**, 53–98 (1979)
Flaherty, J.E., Hoppensteadt, F.C.: Frequency entrainment of a forced van der Pol oscillator. Stud. Appl. Math. **58**, 5–15 (1978)
Gelfreich, V.G.: Melnikov method and exponentially small splitting of separatrices. Phys. D **101**, 227–248 (1997)
Golubitsky, M., Stewart, I., Schaeffer, D.G.: Singularities and Groups in Bifurcation Theory. Springer, Berlin (1988)
Guckenheimer, J., Holmes, P.: Nonlinear Oscillations, Dynamical Systems, and Bifurcations of Vector Fields. Springer, Berlin (1983)
Guckenheimer, J., Hoffman, K., Weckesser, W.: The forced van der Pol equation I: the slow flow and its bifurcations. SIAM J. Appl. Dyn. Syst. **2**, 1–35 (2003)
Haiduc, R.: Horseshoes in the forced van der Pol system. Nonlinearity **22**, 213–237 (2009)
Han, X., Bi, Q.: Slow passage through canard explosion and mixed-mode oscillations in the forced Van der Pol's equation. Nonlinear Dyn. **68**, 275–283 (2012)
Izhikevich, E.M.: Neural excitability, spiking and bursting. Int. J. Bifurc. Chaos **10**, 11711266 (2000)
Izhikevich, E.: Synchronization of elliptic bursters. SIAM Rev. **43**, 315–344 (2001)
Jones, C.K.R.T.: Geometric singular perturbation theory. In: Johnson, R. (ed.) Dynamical Systems. Lecture Notes in Mathematics, pp. 44–120. Springer, New York (1995)
Kramer, M.A., Traub, R.D., Kopell, N.J.: New dynamics in cerebellar Purkinje cells: torus canards. Phys. Rev. Lett. **101**, 068103 (2008)

Krupa, M., Szmolyan, P.: Extending geometric singular perturbation theory to nonhyperbolic points—fold and canard points in two dimensions. SIAM J. Math. Anal. **33**, 286–314 (2001)
Krupa, M., Wechselberger, M.: Local analysis near a folded saddle-node singularity. J. Differ. Equ. **248**, 2841–2888 (2010)
Kuehn, C.: From first Lyapunov coefficients to maximal canards. Int. J. Bifurc. Chaos **20**, 1467–1475 (2010)
Kuehn, C.: Multiple Time Scale Dynamics. Springer, Berlin (2015)
Lanford, O.E., III: Bifurcation of periodic solutions into invariant tori: the work of Ruelle and Takens. In: Nonlinear Problems in the Physical Sciences and Biology, pp. 159–192. Springer, Berlin (1973)
Levi, M.: Qualitative analysis of the periodically-forced relaxation oscillations. Mem. AMS **32**, 244 (1981)
Levinson, N.: A second-order differential equation with singular solutions. Ann. Math. **50**(1), 127–153 (1949)
Mitry, J., McCarthy, M., Kopell, N., Wechselberger, M.: Excitable neurons, firing threshold manifolds and canards. J. Math. Neurosci. **3**, 12 (2013)
Roberts, K.-L., Rubin, J., Wechselberger, M.: Averaging, Folded Singularities, and Torus Canards: Explaining Transitions Between Bursting and Spiking in a Coupled Neuron Model. SIAM J. Appl. Dyn. Syst. **14**, 1808–1844 (2015)
Rotstein, H., Wechselberger, M., Kopell, N.: Canard induced mixed-mode oscillations in a medial entorhinal cortex layer II stellate cell model. SIAM J. Appl. Dyn. Syst. **7**, 1582–1611 (2008)
Rubin, J., Wechselberger, M.: The selection of mixed-mode oscillations in a Hodgkin–Huxley model with multiple timescales. Chaos **18**, 015105 (2008)
Sanders, J.A., Verhulst, F.: Averaging Methods in Nonlinear Dynamical Systems. Springer, Berlin (1985)
Sekikawa, M., Inaba, N., Yoshinaga, T., Kawakami, H.: Collapse of duck solution in a circuit driven by an extremely small periodic force. Electron. Comm. Jpn. Part 3 **88**(4), 199–207 (2005)
Szmolyan, P., Wechselberger, M.: Canards in $\mathbb{R}^3$. J. Differ. Equ. **177**, 419–453 (2001)
Szmolyan, P., Wechselberger, M.: Relaxation oscillations in $\mathbb{R}^3$. J. Differ. Equ. **200**, 69–104 (2004)
Teka, W., Tabak, J., Vo, T., Wechselberger, M., Bertram, R.: The dynamics underlying pseudo-plateau bursting in a pituitary cell model. J. Math. Neurosci. **1**, 12 (2011)
van der Pol, B.: A theory of the amplitude of free and forced triode vibrations. Radio Rev. **1**, 701–710, 754–762 (1920)
van der Pol, B.: Forced oscillations in a circuit with non-linear resistance (reception with reactive triode). Lond. Edinb. Dublin Phil. Mag. J. Sci. Ser. 7, **3**, 65–80 (1927)
Vo, T., Wechselberger, M.: Canards of folded saddle-node type I. SIAM J. Math. Anal. **47**, 3235–3283 (2015)
Wechselberger, M.: Existence and bifurcation of canards in $\mathbb{R}^3$ in the case of a folded node. SIAM J. Appl. Dyn. Syst. **4**, 101–139 (2005)
Wechselberger, M.: À propos de canards (apropos canards). Trans. Am. Math. Soc. **364**, 3289–3309 (2012)
Wechselberger, M., Mitry, J., Rinzel, J.: Canard theory and excitability. In: Nonautonomous Dynamical Systems in the Life Sciences, Lecture Notes in Mathematics, vol. 2102 (Mathematical Biosciences Subseries) (2014)